Available online at www.sciencedirect.com

ScienceDirect

Geochimica et Cosmochimica Acta 232 (2018) 101–123

Geochimica et Cosmochimica Acta

www.elsevier.com/locate/gca

Effect of silicon on activity coefficients of siderophile elements (Au, Pd, Pt, P, Ga, Cu, Zn, and Pb) in liquid Fe: Roles of core formation, late sulfide matte, and late veneer in shaping terrestrial mantle geochemistry

K. Righter [a,*], K. Pando [b], M. Humayun [c], N. Waeselmann [c], S. Yang [c], A. Boujibar [a,1], L.R. Danielson [b]

[a] *NASA JSC, Mailcode XI2, 2101 NASA Pkwy, Houston, TX 77058, United States*
[b] *Jacobs JETS Contract, NASA JSC, Houston, TX 77058, United States*
[c] *National High Magnetic Field Laboratory, Florida State Univ., Tallahassee, FL 32310, United States*

Received 23 October 2017; accepted in revised form 9 April 2018; available online 21 April 2018

Abstract

Earth's core contains ~10% of a light element that may be a combination of Si, S, C, O or H, with Si potentially being the major light element. Metal-silicate partitioning of siderophile elements can place important constraints on the P-T-fO_2 and composition of the early Earth, but the effect of Si alloyed in Fe liquids is unknown for many of these elements. In particular, the effect of Si on the partitioning of highly siderophile elements (Au, Re and PGE) is virtually unknown. To address this gap in understanding, we have undertaken a systematic study of the highly siderophile elements Au, Pd, and Pt, and the volatile siderophile elements P, Ga, Cu, Zn, and Pb at variable Si content of metal, and 1600 °C and 1 GPa. From our experiments we derive epsilon interaction parameters between these elements and Si in Fe metallic liquids. The new parameters are used to update an activity model for trace siderophile elements in Fe alloys; Si causes large variation in the magnitude of activity coefficients of these elements in FeSi liquids. Because the interaction parameters are all positive, Si causes a decrease in their metal/silicate partition coefficients. We combine these new activity results with experimental studies of Au, Pd, Pt, P, Ga, Cu, Zn and Pb, to derive predictive expressions for metal/silicate partition coefficients which can then be applied to Earth. The expressions are applied to two scenarios for continuous accretion of Earth; specifically for constant and increasing fO_2 during accretion. The results indicate that mantle concentrations of P, Ga, Cu, Zn, and Pb can be explained by metal-silicate equilibrium during accretion of the Earth where Earth's early magma ocean deepens to pressures of 40–60 GPa. Au, Pd, and Pt, on the other hand become too high in the mantle in such a scenario, and require a later removal mechanism, rather than an addition as traditionally argued. A late reduction event that removes 0.5% metal from a shallow magma ocean can lower the Au, Pd, and Pt contents to values near the current day BSE. On the other hand, removal of 0.2–1.0% of a late sulfide-rich matte to the core would lower the Au, Pd, and Pt concentrations in the mantle, but not to chondritic relative concentrations observed in the BSE. If sulfide matte is called upon to remove HSEs, they must be later added via a late veneer to re-establish the high and chondritic relative PUM concentrations. These results suggest that although accretion and core formation (involving a Si, S, and C-bearing metallic liquid) were the primary processes establishing many of Earth's mantle volatile elements and HSE, a secondary removal process is required to establish HSEs at their current and near-chondritic relative BSE levels. Mn and P - two siderophile elements that are central to biochemical processes (photosynthesis and triphosphates,

* Corresponding author.
E-mail address: kevin.righter-1@nasa.gov (K. Righter).
[1] Current address: Geophysical Laboratory, Carnegie Institution for Science, 5251 Broad Branch Road NW, Washington DC 20015-1305, United States.

https://doi.org/10.1016/j.gca.2018.04.011
0016-7037/Published by Elsevier Ltd.

respectively) - have significant and opposite interactions with FeSi liquids, and their mantle concentrations would be notably different if Earth had a Si-free core.
Published by Elsevier Ltd.

Keywords: Core formation; Accretion; Late veneer; Siderophile elements; Chalcophile elements

1. INTRODUCTION

Siderophile elements can provide important constraints on the conditions of accretion and core formation in the early Earth, and in particular the temperature, pressure, oxygen fugacity, and metallic and silicate liquid compositions. The relative importance of all these variables is different for each element, and in particular the non-metal content of the metallic liquid can exert a strong influence on the magnitude of D(metal/silicate), defined as the concentration (i) in metal/concentration (i) in silicate, the partition coefficient of siderophile elements between the core and mantle. Earth's core contains ~10% light elements that are likely a combination of S, C, Si, and O, with Si possibly being the most abundant (e.g., Hirose et al., 2013). Many recent studies have focused on Si as the major light element in the core (and C and S being minor), using a variety of approaches such as seismology (Lin et al., 2003; Sanloup et al., 2004; Badro et al., 2007; Mao et al., 2012), high pressure experimentation (Ricolleau et al., 2011; Siebert et al., 2013; Fischer et al., 2015) and isotopic and cosmochemical arguments (Georg et al., 2007; Ziegler et al., 2010). The effect of S and C on metal/silicate partitioning is relatively well understood for many moderately siderophile elements (e.g., Chabot et al., 2006; Siebert et al., 2011; Wood et al., 2014), and highly siderophile elements (e.g., Laurenz et al., 2016; Righter et al., 2015), but the effect of Si alloyed with Fe liquid is relatively poorly understood. There are some insights from solid/liquid metal partitioning such as Chabot et al. (2010) for Si. Although the effect of Si on partitioning of Ge, As, and Sb are in agreement with the Chabot et al. (2010) work, there are differences for some elements such as Mo and W, suggesting that the solid/liquid metal systems may not always be an accurate guide to behavior in metal-silicate systems. Some work in metal-silicate systems has also been undertaken. The effect of Si can be small such as for Ni and Co (e.g., Tuff et al., 2011), or large such as for Mo, Ge, Sb, and As (e.g., Righter et al., 2016a, 2017), but its effect on many other siderophile elements in metal-silicate systems is unknown, yet could be an important influence on the core-mantle partitioning of SE. Here we report new experiments designed to quantify the effect of Si on the partitioning of P, Au, Pd, Pt, Zn, Cu, Pb, and Ga and several other SE between metal and silicate melt. The results will be applied to Earth, for which we have constraints on the mantle siderophile element concentrations from analyses of peridotite xenoliths and massifs.

2. EXPERIMENTAL

Experiments were carried out using a non end loaded piston cylinder apparatus and run conditions of 1 GPa and 1600 °C. Samples were heated with a graphite furnace, with temperature monitored with a Type C W-Re thermocouple. Pressure was generated using a $BaCO_3$ medium, calibrated against the melting point of diopside. The starting materials comprised basaltic silicate (70% by mass; Knippa basalt; Lewis et al., 1993) mixed with metal of three different compositions (and hence three different series): metallic Fe + 5% Au, metallic Fe + 5% Pd, or metallic Fe + 5% Pt. Silicon metal was also added to the metallic mixture at 2, 4, 6, and 10%, to create a variable amount of Si alloyed with Fe in each series. The metal mixtures were added as 30% by mass. These metal-silicate mixtures were then placed in sintered MgO capsules, and at run conditions, the MgO capsule reacts with the silicate melt to form more MgO-rich liquids that have 22–26 wt% MgO. Samples were held at run conditions for 90 min at 1600 °C, to ensure approach to equilibrium, with the duration determined by a previously completed series of experiments on siderophile elements (Righter et al., 2017).

3. ANALYTICAL

Experimental metals and silicates were analyzed using a combination of electron microprobe analysis (EMPA) at NASA-JSC, and laser ablation ICP-MS at Florida State University.

EMPA analysis (using both Cameca SX100 and JEOL 8530 FEG microprobes) was used for major and minor elements (Fe, Si, P, Au, Pd, Pt, and S) and utilized a variety of mineral and glass standards with 15 kV and 20 nA conditions (Tables 1–3). Trace elements (typically those < 100 ppm; Ga, Zn, Cu, Pb, Au, Pd, Pt, V, Cr, Ni, Co, Ag) were measured with LA-ICP-MS using glass and metal standards and either spot or line analyses depending on the size of the metal or silicate regions of interest (Tables 1–3).

Each sample was analyzed by an ElectroScientific Instruments (ESI) New Wave UP193FX excimer (193 nm) laser ablation system coupled to a Thermo Element XR Inductively Coupled Plasma Mass Spectrometer (ICP-MS) at the Plasma Analytical Facility of the National High Magnetic Field Laboratory, Florida State University, for: ^{29}Si, ^{31}P, ^{51}V, ^{53}Cr, ^{55}Mn, ^{57}Fe, ^{59}Co, ^{60}Ni, ^{63}Cu, ^{66}Zn, ^{71}Ga, $^{105+106}Pd$, ^{193}Ir, ^{195}Pt, ^{197}Au, ^{208}Pb, and other elements as described by Yang et al. (2015). Internal standards were ^{29}Si for silicates and ^{57}Fe for metal + sulfide. The relevant isobaric interferences are discussed in Yang et al. (2015). Laser fluence was 2 GW/cm^2. Relative sensitivity factors were obtained using NIST SRM 610 glass, USGS Basaltic Glasses BHVO-2G, BIR-1G, and BCR-2G for lithophile elements (Jochum et al., 2011), and Hoba IVB (Walker et al., 2008) and Filomena IIA (Wasson et al., 1989) for siderophile elements (Humayun et al., 2007; Gaboardi and Humayun, 2009; Humayun, 2012). The metal portions of

Table 1
Summary of Au experiments (1 GPa, 1600 °C) and EMPA and LA-ICP-MS analyses.

Silicate EMPA – wt%							
	Au0	Au2	Au6	Au10	Au4B	Au6B	Au10B
SiO_2	28.9(1.4)	30.4(1.5)	31.8(1.6)	39.4(2.0)	42.3(2.1)	43.7(2.2)	44.2(2.2)
TiO_2	2.89(6)	2.81(6)	4.33(9)	2.71(5)	3.53(7)	3.37(7)	2.07(4)
Al_2O_3	8.7(4)	8.9(4)	11.3(6)	8.1(4)	11.5(6)	12.0(6)	11.9(6)
FeO	10.37(21)	7.68(15)	4.04(8)	0.48(1)	0.100(1)	0.030(1)	0.010(1)
MnO	0.140(1)	0.150(1)	0.150(1)	0.140(1)	0.120(1)	0.080(1)	0.030(1)
MgO	33.4(1.7)	35.0(1.8)	26.9(1.4)	35.7(1.8)	25.2(1.3)	22.4(1.1)	23.2(1.2)
CaO	10.83(22)	10.64(21)	15.88(32)	9.83(20)	12.46(25)	13.37(27)	13.11(26)
Na_2O	2.6(1)	2.6(1)	3.4(2)	2.4(1)	3.4(2)	3.7(2)	3.7(2)
K_2O	1.47(3)	1.47(3)	1.98(4)	1.32(3)	1.96(4)	2.22(4)	2.13(4)
P_2O_5	0.26(1)	0.48(1)	0.26(1)	0.006(1)	0.020(1)	0.020(1)	0.010(1)
Total	99.57	99.97	99.97	99.97	100.55	100.91	100.34
Silicate LA-ICP-MS – ppm							
V	181(18)	161(16)	201(20)	113(11)	17(2)	4.0(4)	1.0(1)
Cr_2O_3 (wt%)	0.024(2)	0.021(2)	0.023(2)	0.015(2)	0.0040(4)	0.0020(2)	0.0010(1)
Co	0.36(4)	0.31(3)	0.59(6)	0.19(2)	n.d.	n.d.	n.d.
Ni	20.5(2.0)	25.2(2.5)	87(9)	28(3)	0.70(7)	0.20(2)	0.70(7)
Cu	2.9(3)	2.5(3)	2.4(2)	0.77(8)	0.80(8)	1.0(1)	19.7(2.0)
Zn	54.3(5.4)	46.2(4.6)	40.2(4.0)	13.1(1.3)	5.3(5)	4.2(4)	4.5(4)
Ga	8.0(8)	6.7(7)	4.3(4)	2.5(3)	4.2(4)	5.5(6)	5.3(5)
Ag	0.11(1)	0.12(1)	0.062(6)	0.044(4)	0.032(3)	0.066(7)	0.15(2)
Au	4.59(46)	3.22(32)	2.73(27)	1.7(2)	5.52(55)	13.8(1.4)	16.1(1.6)
Pb	1.2(1)	0.91(9)	0.68(7)	0.099(9)	0.041(4)	0.043(4)	0.096(9)
Metal EMPA – wt%							
Si	0.020(4)	n.d.	n.d.	0.160(3)	3.12(6)	8.13(16)	15.86(32)
P	0.200(4)	0.290(6)	0.64(1)	0.86(2)	0.70(1)	0.66(1)	0.72(1)
Au	5.95(11)	5.06(10)	4.59(9)	4.61(9)	3.84(8)	2.71(5)	2.10(4)
Pd	n.d.	n.d.	n.d.	n.d.	n.d.	n.d.	n.d.
Fe	90.76(1.82)	91.50(1.83)	93.30(1.87)	92.42(1.84)	91.54(1.83)	87.43(1.75)	79.03(1.58)
Ni	0.070(1)	0.070(1)	0.070(1)	n.d.	n.d.	n.d.	n.d.
Metal LA-ICP-MS – ppm							
V	n.d.	n.d.	n.d.	303(30)	477(48)	500(50)	500(50)
Cr	n.d.	n.d.	83(8)	587(60)	675(68)	731(73)	860(86)
Mn	n.d.	n.d.	42(4)	325(33)	1065(107)	2736(274)	5385(540)
Co	145(15)	137(14)	122(12)	124(12)	111(11)	105(11)	123(12)
Ni	655(66)	708(71)	603(60)	526(53)	513(51)	481(48)	563(56)
Cu	235(24)	182(18)	153(15)	164(16)	155(16)	206(21)	243(24)
Zn	62(6)	56(6)	120(12)	340(34)	386(39)	556(56)	690(69)
Ga	29(3)	31(3)	37(4)	41(4)	38(4)	45(5)	72(7)
Ag	9.2(9)	5.5(5)	4.6(5)	4.5(5)	4.2(4)	7.9(8)	9.8(9)
Pb	33(3)	24(2)	15(2)	19(2)	18(2)	28(3)	36(4)
Total	97.12	97.03	98.73	98.29	99.54	99.47	98.56
Δ IW^{ideal}	−1.96	−2.26	−2.80	−4.70	−6.00	−6.99	−7.83
Δ $IW^{activity}$	−1.46	−1.72	−2.15	−3.98	−5.21	−6.14	−6.82
nbo/t	3.48	3.32	2.59	2.55	1.75	1.58	1.61
D(Au)	1.3×10^4	1.6×10^4	1.7×10^4	2.7×10^4	7.0×10^3	2.0×10^3	1.3×10^3
(+/−)	0.1×10^4	0.2×10^4	0.2×10^4	0.3×10^4	0.7×10^3	0.2×10^3	0.1×10^3

the samples were measured using a 20 μm raster at 5 μm/s and 20 Hz, collected with 150 runs. Because of the presence of quench olivine and MgO crystals (the latter from reaction with the capsule) scattered throughout, a 50 μm line was scanned at 10 μm/s, 20 Hz, 100 runs. Single values were examined to screen out spikes associated with MgO crystals. The relative standard deviation (RSD) of HSE abundances in metal from each of the runs was ~2%, and RSD of HSE in the silicate portions averaged ~20%.

4. RESULTS

4.1. Phase equilibria and equilibrium

All experiments equilibrated metallic liquid and silicate melt. Because the silicate melts are generally MgO rich (MgO > 20%) they are difficult to quench to a glass even at high quench rates, and so the run products contain a mixture of glass and coarse-grained,

Table 2
Summary of Pd experiments (1 GPa, 1600 °C) and EMPA and LA-ICP-MS analyses.

	Pd0	Pd2	Pd4	Pd6	Pd4B	Pd6B	Pd10B
Silicate EMPA – wt%							
SiO_2	31.1(1.6)	31.2(1.6)	31.6(1.6)	33.5(1.7)	43.7(2.2)	43.3(2.2)	41.6(2.1)
TiO_2	3.70(7)	3.56(7)	3.67(7)	4.44(9)	3.52(7)	3.31(7)	2.02(4)
Al_2O_3	11.2(6)	10.6(5)	11.1(6)	12.7(6)	11.3(6)	11.5(6)	11.9(6)
FeO	11.84(24)	10.29(21)	7.44(15)	5.51(11)	0.140(1)	0.040(1)	0.020(1)
MnO	0.160(1)	0.180(1)	0.160(1)	0.180(1)	0.150(1)	0.090(1)	0.020(1)
MgO	23.2(1.2)	27.1(1.4)	27.8(1.4)	20.6(1.0)	23.4(1.2)	24.2(1.2)	26.2(1.3)
CaO	12.82(26)	12.22(24)	13.84(28)	15.49(31)	12.75(26)	12.69(25)	13.17(26)
Na_2O	3.3(2)	3.0(2)	3.1(2)	4.3(2)	3.4(2)	3.4(2)	3.7(2)
K_2O	1.95(4)	1.73(3)	1.88(4)	2.42(5)	1.95(4)	2.08(4)	2.13(4)
P_2O_5	0.73(1)	0.71(1)	0.52(1)	0.26(1)	0.020(1)	0.020(1)	0.020(1)
Total	99.96	100.62	101.03	99.42	100.35	100.65	100.78
Silicate LA-ICP-MS – ppm							
V	182(18)	209(21)	191(19)	216(22)	24(3)	7.5(7)	1.0(1)
Cr_2O_3 wt%	0.017(2)	0.027(3)	0.018(2)	0.024(2)	0.0072(7)	0.0029(3)	0.00050(5)
Co	0.40(4)	1.8(2)	0.50(5)	8.6(8)	8.0(8)	4.0(4)	0.90(9)
Ni	1.7(2)	1.9(2)	1.0(1)	29.5(3.0)	1.7(2)	0.85(8)	6.0(6)
Cu	2.7(3)	3.1(3)	2.1(2)	3.2(3)	1.5(2)	0.90(9)	0.90(9)
Zn	44.4(4.4)	63.6(6.4)	42.0(4.2)	59.4(5.9)	7.1(7)	4.6(5)	3.3(3)
Ga	8.3(8)	8.7(8)	7.4(7)	4.0(4)	1.7(2)	2.2(2)	4.2(4)
Pd	0.60(6)	5.52(55)	0.38(4)	3.27(33)	3.2(3)	2.7(3)	2.9(3)
Ag	0.047(5)	0.13(1)	0.041(4)	0.53(5)	0.49(5)	0.31(3)	0.042(4)
Pb	0.74(7)	0.94(9)	0.50(5)	0.76(8)	0.046(5)	0.048(5)	0.050(5)
Metal EMPA – wt%							
Si	n.d.	n.d.	n.d.	n.d.	2.85(6)	7.81(16)	15.73(31)
P	0.150(3)	0.230(5)	0.340(7)	0.54(1)	0.73(1)	0.52(1)	0.76(2)
Au	n.d.	n.d.	n.d.	n.d.	0.030(1)	0.030(1)	0.030(1)
Pd	6.02(12)	5.38(11)	4.94(10)	4.61	3.94(8)	3.25(7)	2.79(6)
Fe	93.40 (1.87)	93.89 (1.88)	95.22 (1.90)	93.73 (1.87)	91.81 (1.84)	88.03 (1.76)	78.75 (1.58)
Ni	n.d.	n.d.	n.d.	n.d.	n.d.	n.d.	n.d.
Metal LA-ICP-MS – ppm							
V	9(1)	24(2)	8(1)	15(2)	422(42)	460(46)	605(61)
Cr	37(4)	62(6)	61(6)	100(10)	674(67)	714(71)	790(79)
Mn	60(6)	163(16)	38(4)	61(6)	872(87)	1734(173)	3734(373)
Co	159(16)	135(14)	133(13)	125(13)	115(12)	106(11)	115(12)
Ni	698(70)	597(60)	572(57)	588(60)	536(54)	471(47)	497(50)
Cu	220(22)	200(20)	192(19)	203(20)	178(18)	156(16)	149(15)
Zn	88(9)	85(8)	121(12)	170(17)	381(38)	367(37)	568(57)
Ga	35(4)	38(4)	39(4)	47(5)	46(5)	43(4)	48(5)
Ag	0.20(2)	0.20(2)	0.30(3)	0.90(9)	0.60(6)	0.20(2)	0.20(2)
Pb	15(2)	16(2)	15(2)	23(2)	22(2)	17(2)	21(2)
Total	99.70	99.63	100.62	99.03	99.68	100.05	98.71
Δ IW^{ideal}	−1.79	−1.96	−2.27	−2.49	−5.69	−6.73	−7.22
Δ IW^{activity}	−1.29	−1.41	−1.67	−1.83	−4.91	−5.88	−6.20
nbo/t	2.52	2.72	2.69	2.07	1.66	1.63	1.67
D(Pd)	1.0×10^5	9.7×10^3	1.3×10^5	1.4×10^4	1.2×10^4	1.2×10^4	9.5×10^3
(±)	0.1×10^5	1.0×10^3	0.1×10^5	0.1×10^4	0.1×10^4	0.1×10^4	0.9×10^3

skeletal-shaped, quench silicate crystals (Fig. 1). Metallic liquids also do not quench to a glass, but rather a matte of quench crystals. Both phases must be analyzed with a larger beam size and averaged over many points to obtain a representative analysis of the run products. This approach has been discussed and reported in detail by Righter et al. (2017). Some studies of HSEs report the stability and existence of micronuggets of the HSE metal, such as Pt or Pd (e.g., Malavergne et al., 2016; Ertel et al., 2006). We observed no HSE micronuggets in our experiments (Fig. S1; Supplementary Information), and any HSE particles that appeared as "spikes" in the analysis of the glasses could be filtered out during the data reduction, as also explained by Righter et al. (2015).

4.2. Oxygen fugacity

To promote more reduced conditions in the experiments, Si metal was added to the metal phase because increased Si content will cause a decrease in fO_2. Oxygen fugacity was calculated relative to the iron-wüstite (IW) oxygen buffer using the expression $\Delta IW = -2\log [X_{Fe}/X_{FeO}]$. The ΔIW values ranged from ~−1.8 for Si free runs compared to as low as −7.8 for Si bearing runs (Tables 1–3). If activities of Fe and FeO are considered, the equation

Table 3
Pt series.

	Pt0	Pt 2	Pt 4	Pt 6	Pt 10	Pt 4B	Pt 6B	Pt 10B
Silicate EMPA – wt%								
SiO_2	30.5(1.5)	31.2(1.6)	31.6 (1.6)	32.8(1.6)	41.9(2.1)	42.3(2.1)	43.6(2.2)	43.9(2.2)
TiO_2	3.52(7)	3.72(7)	3.73(7)	3.62(7)	3.67(7)	3.61(7)	3.45(7)	2.15(4)
Al_2O_3	10.5(5)	11.7(6)	11.9(6)	11.9(6)	12.3(6)	11.5(6)	12.1(6)	11.8(6)
FeO	12.35(25)	9.83(20)	8.11(16)	5.34(11)	0.67(01)	0.110(1)	0.030(1)	0.010(1)
MnO	0.160(1)	0.160(1)	0.170(1)	0.170(1)	0.170(1)	0.120(1)	0.080(1)	0.030(1)
MgO	24.2(1.2)	23.0(1.2)	25.5(1.3)	28.8(1.4)	24.0(1.2)	25.1(1.3)	22.3(1.1)	23.3(1.2)
CaO	12.18(24)	13.57(27)	13.53(27)	12.68(25)	13.08(26)	12.38(25)	13.25(27)	13.22(26)
Na_2O	3.6(2)	4.0(2)	3.7(2)	3.4(2)	3.5(2)	3.5(2)	3.7(2)	3.7(2)
K_2O	1.94(4)	2.25(5)	2.06(4)	2.04(4)	1.99(4)	1.95(4)	2.18(4)	2.09(4)
P_2O_5	0.71(1)	0.67(1)	0.64(1)	0.40(1)	0.030(1)	0.020(1)	0.020(1)	0.010(1)
Total	99.65	100.17	100.92	101.21	101.23	100.54	100.69	100.2
Silicate LA-ICP-MS - ppm								
Pt	5.1(5)	4.5(5)	4.7(5)	4.2(4)	4.1(4)	3.6(4)	3.2(3)	3.0(3)
Metal EMPA – wt%								
Si	0.020(2)	0.020(2)	0.020(2)	0.020(2)	0.230(2)	2.77(6)	8.47(17)	17.57(35)
Fe	95.0(1.9)	95.0(1.9)	95.0(1.9)	93.73(1.87)	93.34(1.87)	91.81(1.84	88.03(1.76)	78.75(1.58)
P	0.100(1)	0.170(1)	0.240(2)	0.64(1)	0.89(2)	0.67(1)	0.842)	0.57(1)
Pt	5.11(10)	4.45(9)	4.7(9)	4.2(8)	4.1(8)	3.6(7)	3.2(6)	3.0(6)
Total	100.23	99.64	99.96	98.62	98.52	98.89	100.53	99.86
Δ IW^{ideal}	−1.83	−2.00	−2.29	−2.51	−4.45	−5.71	−6.73	−7.19
Δ IW^{activity}	−1.30	−1.47	−1.59	−1.93	−3.66	−5.15	−6.12	−6.77
nbo/t	2.69	2.45	2.50	2.50	1.70	1.75	1.56	1.62
D(Pt)	3.4×10^6	2.0×10^6	7.7×10^6	5.9×10^6	6.3×10^6	8.0×10^5	5.8×10^5	9.6×10^5
(±)	0.3×10^6	0.2×10^6	0.8×10^6	0.6×10^6	0.6×10^6	0.8×10^5	0.6×10^5	1.0×10^5

becomes $\Delta IW = -2\log [a_{Fe}/a_{FeO}]$. In this case a_{Fe} is calculated using the epsilon interaction parameter model for metallic liquids (see Supplementary Information), and a_{FeO} can be calculated in silicate melt using the results of Holzheid et al. (1997). ΔIW values calculated using activities instead of mole fractions are slightly higher, ranging from IW-1.3 to -6.8 (Tables 1–3). Because most studies utilize the first approach, we include those in the tables and figures, but it is important to note the difference in these approaches given the non-ideality in the Fe-Si system; activities are used in all calculations. The range of ΔIW values for these experiments falls in the range typically considered during Earth's core formation.

4.3. Comparison of partition coefficients to previous work and Henry's Law considerations

The partition coefficients for the Si-free experiments reported here are near 10^4 for Au and 10^5 for Pd and Pt. These values are in close agreement with the previous results for Si-free Fe metallic liquids at the same or similar conditions reported by Brenan and McDonough (2009), Wheeler et al. (2011), Mann et al. (2012) and Righter et al. (2015). Similarly, the results for Ga, Cu, Zn and P reported here in the experiments with Si-free metallic liquids, are in agreement with results reported by Corgne et al. (2008), Righter et al. (2010), and Siebert et al. (2011), with $D(Ga) \sim 1$–4, $D(Cu) \sim 40$–60, $D(Zn) \sim 1$–1.3, and $D(P) \sim 0.2$–0.5. The results at lower fO_2, however, deserve some description and explanation. Traditionally, partition coefficients at low fO_2 (<IW-4) are expected to be higher than those at high fO_2, with the extent of the increase dependent directly on the valence (n) of the element, by a factor of n/4 for each $\log fO_2$ unit (e.g., Capobianco et al., 1999). This can be seen in several datasets across a wide fO_2 range (e.g., Newsom and Drake, 1983; Holzheid and Palme, 1996). However, at very low fO_2, Si alloys with Fe liquid, and the activities of trace elements are strongly affected by the Si (e.g., Tuff et al., 2011; Righter et al., 2017), and the traditional slope of partition coefficient and $\log fO_2$ does not hold. This can also be true of Fe-Ni alloys (Capobianco et al., 1999). In these cases, and also in the present study, the trends of D(metal/silicate) vs. $\log fO_2$ are not only affected, but the partition coefficient can still be quite low at low fO_2 due to the effects of Si. The exchange coefficient of a trace element between metal and silicate melt is constant at fixed T and P, and independent of fO_2 as long as there are no valence changes in the trace metal. Therefore, in this study, the deviation from the expected lnK with variable Si content can be used to calculate the activity coefficient for a trace element in FeSi liquids, as will be explained in the next section.

The concentration levels of Ga, Cu, Zn, Pb, and P in the metals are low and close to natural levels, whereas the Au, Pd, and Pt concentrations are higher and present at several wt%. The activity coefficient approach used below utilizes a correction to infinite dilution, so the metals in these experiments do not need to be corrected for non-Henrian behavior – this is accounted for in the activity treatment (see Supplementary information).

4.4. Determination of epsilon interaction parameters

Measured P, Au, Pd, Pt, and other siderophile elements were used to calculate metal (met) - silicate (sil) exchange K_d according to this equation:

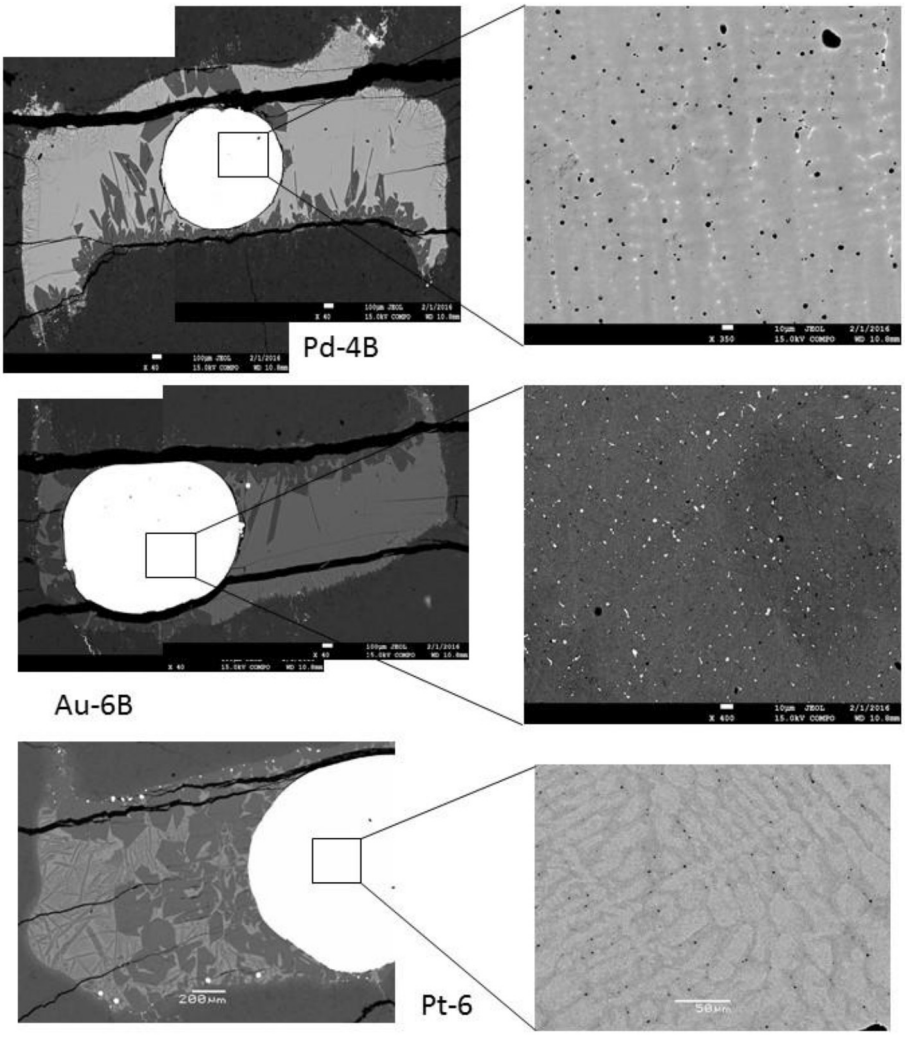

Fig. 1. BSE images of Pd-4B, Au-6B, and Pt-6. For each experiment, images on the left show the bright white metallic liquid, and lighter gray silicate melts which mostly quenched to glass (but there are regions where quench crystals formed in the glass, too). Images on the right show close up of phases in the quenched metallic liquids. All experiments were carried out in MgO capsules, which reacted slightly with the silicate melt.

$$MOn/2_{\text{sil}} + (n/2)\text{Fe}_{\text{met}} = M_{\text{met}} + (n/2)\text{FeO}_{\text{sil}} \quad (1)$$

Expanding Eq. (1),

$$\ln K = \ln \frac{[a_M^{metal}][a_{FeO}^{silicate}]^{n/2}}{[a_{MO(n/2)}][a_{Fe}^{metal}]^{n/2}} = \ln \frac{[X_M^{metal}][X_{FeO}^{silicate}]^{n/2}}{[X_{MO(n/2)}^{silicate}][X_{Fe}^{metal}]^{n/2}} + \ln \frac{[\gamma_M^{metal}][\gamma_{FeO}^{silicate}]^{n/2}}{[\gamma_{MO(n/2)}][\gamma_{Fe}^{metal}]^{n/2}} \quad (2)$$

We set $K_d = \frac{[X_M^{metal}][X_{FeO}^{silicate}]^{n/2}}{[X_{MO(n/2)}^{silicate}][X_{Fe}^{metal}]^{n/2}}$ and following a similar approach to Wood et al. (2014), we assume the ratio of oxide activity coefficients in the silicate, $\frac{[\gamma_{FeO}^{silicate}]}{[\gamma_{MO(n/2)}^{silicate}]}$, is constant since the silicate melt compositions are nearly constant in this study. On the other hand, the metal composition varies significantly in Si content and the ratio of activity coefficients in the metal, $\frac{[\gamma_M^{metal}]}{[\gamma_M^{metal}]^{n/2}}$, is dependent upon variation in metal composition. The above equations can be re-arranged to yield:

$$\ln K_d = \text{constant} + \text{n}/2 \ln \gamma_{Fe}^{metal} - \ln \gamma_M^{metal} \quad (3)$$

When (3) is combined with $\ln \gamma_M^{metal} = \ln \gamma_{Fe}^{metal} + \ln \gamma_M^0 - \varepsilon_M^{Si} \ln(1 - \text{X}_{\text{Si}})$ it becomes

$$\ln K_d - (\text{n}/2 - 1) \ln \gamma_{Fe}^{metal} = \text{const} - \ln \gamma_M^0 + \varepsilon_M^{Si} \ln(1 - \text{X}_{\text{Si}}) \quad (4)$$

Here γ_M^0 is the activity coefficient of M at infinite dilution, γ_{Fe}^{metal} is the activity coefficient of Fe in Fe metal (calculated as described in the Supplementary Information), and ε_M^{Si} is an interaction parameter (e.g., Lupis, 1983) that can be used to isolate the effect of a solute such as Si (in Fe metallic liquid) on the activity of a trace element such as

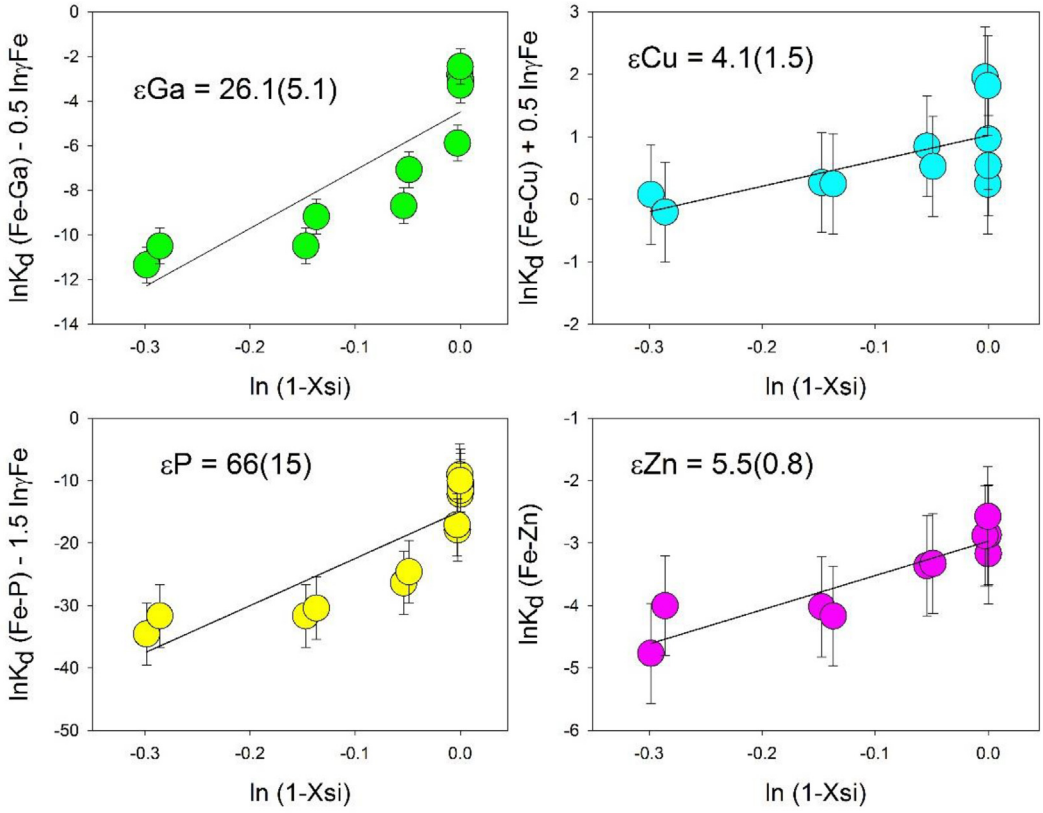

Fig. 2. $\ln K_d$(Fe-P)–1.5ln(γ_{Fe}), $\ln K_d$(Fe-Ga)–0.5ln(γ_{Fe}), $\ln K_d$(Fe-Zn), and $\ln K_d$(Fe-Cu) + 0.5ln(γ_{Fe}) versus ln(1−X_{Si}) from experiments across a wide range of Si contents in metallic Fe. The slope of the lines yields the interaction parameter for each – ε_P, ε_{Ga}, ε_{Zn}, and ε_{Cu} - in Fe-Si liquids.

As, Sb, Ge, and In (Righter et al., 2017). The slope of $\ln K_d$ versus ln(1-X_{Si}) gives ε_M^{Si} directly for each element at 1600 °C.

Using this approach, we have determined ε_M^{Si} for a large number of siderophile elements, including P, Au, Pd, Pt, Ga, Cu, Zn, and Pb, by a linear fit to the data, with the standard error (in parentheses below) and the fits passing variance tests in SigmaPlot 12.0. Phosphorus data combined from the three series of experiments all at 1600 °C and in MgO capsules yield an epsilon interaction parameter of 66(15) (Fig. 2). Gold, Pd, and Pt have positive epsilon parameters, 21.2(3.4), 17.4(8.0), and 27.4(8.2), respectively, indicating that dissolved Si causes a decrease in their partition coefficients (Fig. 3). Ga, Cu, Zn and Pb all have positive epsilon values, also indicating that dissolved Si causes a decrease in the partition coefficients; values are 26.1(5.1), 4.1(1.5), 5.5(0.8) and 11.2(1.3), respectively, at 1 GPa and 1600 °C (Figs. 2 and 3). Ni, Co, and Cr all have positive epsilon values of 13.8(3.8), 14.7(7.7), and 5.0(1.7), respectively, again indicating that dissolved Si causes a decrease in the partition coefficients. Vanadium and Mn, on the other hand, have negative epsilon parameters of −1.4(1.2) and −3.8(1.2), respectively, indicating that Si will cause a very slight increase in D(V) and D(Mn) metal/silicate with Si present in the metallic liquid (Fig. 4). Several elements – Au, Pd, P and Ga – exhibit non-linear behavior, so we also fit these elements to low- and high-Si regions and use them in modelling (see Supplementary data).

4.5. Comparison to previous work, and to interaction parameters for Fe-S metallic liquids

Comparison of our newly determined epsilon parameters to previous studies shows overall agreement between values measured by Tuff et al. (2011) for Ni (7.5), Co (4.6), V (2), Cr (0.03), and Ga (9.98), (Tuff et al., 2011; Blanchard et al., 2015). These values are similar to, or slightly lower than (within error), the values measured in this study, with the differences likely due to calculation procedure or slight differences in melt composition. Our new values for P, Cu, Zn, Ga, Au, Pd, Pt, and Pb demonstrate that *D*(metal/silicate) will be reduced for all elements with the addition of Si to the metallic liquid. Furthermore, the effect of Si is much stronger than S for P, Au, Pd, Pt, In, Ge, Sb, As, Ga, Ni, Co, and for Cu, Zn, and Pb, Si causes a decrease in *D*(metal/silicate) whereas S causes an increase (i.e., these are truly chalcophile elements; Fig. 5).

4.6. Calculation of activity coefficients in Fe-Ni-Si-C-S liquids

The activity model of Ma (2001) and Wade and Wood (2005) was coded in MATLAB, and expanded to include the newly acquired epsilon interaction parameters in Fe-Si liquids for Au, Pd, Pt, P, Ga, Cu, Zn, and Pb obtained here, and for As, Sb, Ge, and In (Righter et al., 2017), as well as previously determined epsilon parameters for S and C for

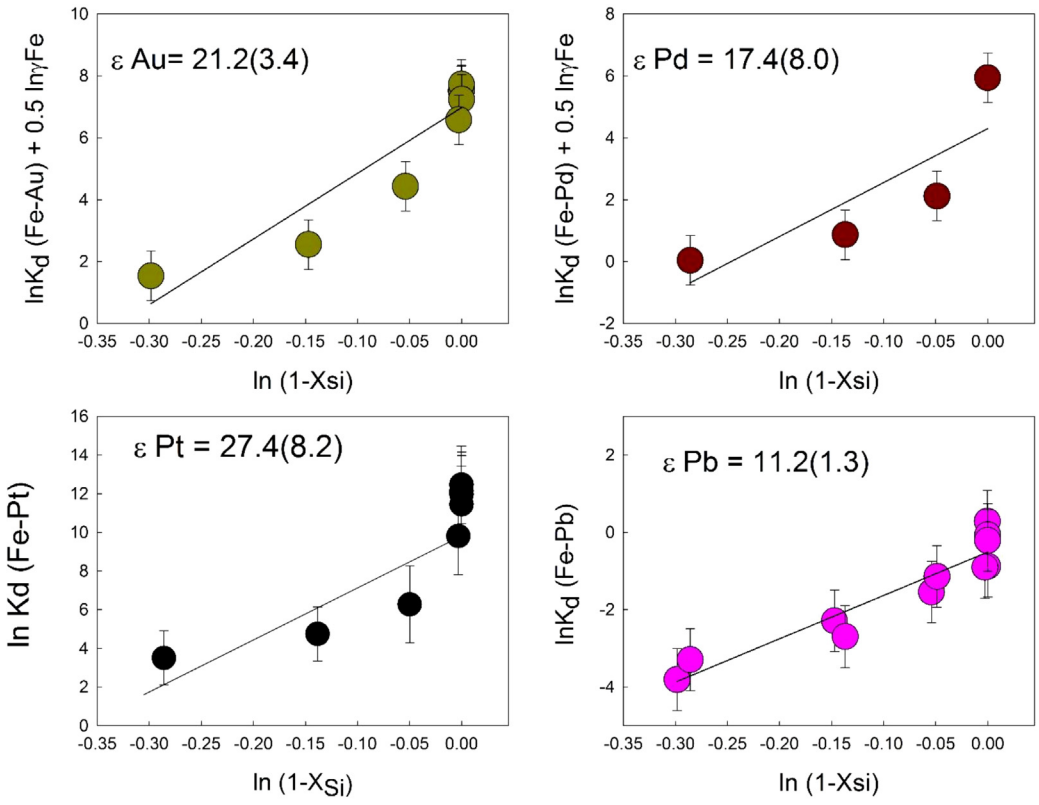

Fig. 3. $\ln K_d$(Fe-Au) + 0.5ln(γ_{Fe}), $\ln K_d$(Fe-Pd) + 0.5ln(γ_{Fe}), $\ln K_d$(Fe-Pt), and $\ln K_d$(Fe-Pb) versus ln(1-X_{Si}) from experiments across a wide range of Si contents in metallic Fe. The slope of the lines yields the interaction parameter for each – ε_{Au}, ε_{Pd}, ε_{Pt}, and ε_{Pb} - in Fe-Si liquids.

these elements (Steelmaking Data Sourcebook, 1988; Wood et al., 2014). This updated model allows us to calculate the activity of Au, Pd, Pt, P, Ga, Cu, Zn, Pb, Ge, In, As, and Sb in Fe-Ni-Si-S-C metallic liquids. As an example of how large the effect of Si can be, these epsilon values correspond to activity coefficients (γ) for Zn and Ga, for example of ~1 when $X_{Si} = 0$, up to $\gamma \sim 3$ when $X_{Si} = 0.2$ (Fig. 6). Similarly, γ increases by a factor of nearly 10 across this range for Cu, Au, Pd, and Pt, and changes by 6 orders of magnitude for P due to the large interaction parameter for P measured in this study. It is clear that Si has an enormous effect on the activity coefficient and metal-silicate partitioning behavior of P.

Why does Si have a large effect on the activity coefficient? Righter et al. (2017) argued that lower epsilon values may be expected for elements that have a greater tendency to form silicides such as Mn, Ni, Cu, Au and Pd, whereas higher epsilon values may be expected for elements that have a lower tendency to form silicides. Support for this comes from Bi, Sn, Ga, Sb, and In, none of which form silicides in M-Si phase diagrams, and all have positive and high values. However, these trends should only be considered a general guide and not a fixed rule as there are some exceptions such as Zn which has a low epsilon value yet also has no silicides in this phase diagram (Olesinski and Abbaschian, 1985).

5. DISCUSSION

5.1. Application to metal/silicate partitioning and core formation in Earth

We combine the new activity model with a compilation of partitioning data for Au, Pd, Pt, P, Ga, Cu, Zn, and Pb, and apply the results to Earth (with a likely Si-rich core) by calculating the resulting mantle concentrations of these elements during a simple continuous accretion model, aspects of which are described below.

5.1.1. Calculating mantle concentrations of siderophile elements

Equilibration occurs instantaneously, so that as Earth grows during accretion there is constant re-equilibration between the core-forming metal and mantle (e.g., Deguen et al., 2014; Kendall and Melosh, 2016). The equation used to calculate mantle concentrations is:

$$C^i_{LS} = \frac{C^i_{bulk}}{x[p + (1-p)D^i_{SS/LS}] + (1-x)[D^i_{LM/LS}]} \quad (5)$$

where x is the fraction of silicate, p is the fraction of molten silicate, C^i_{bulk} is the bulk concentration (by weight) of siderophile element (which here is volatile depleted CI chondrite; see also Righter et al., 2017), C^i_{LS} the concentration

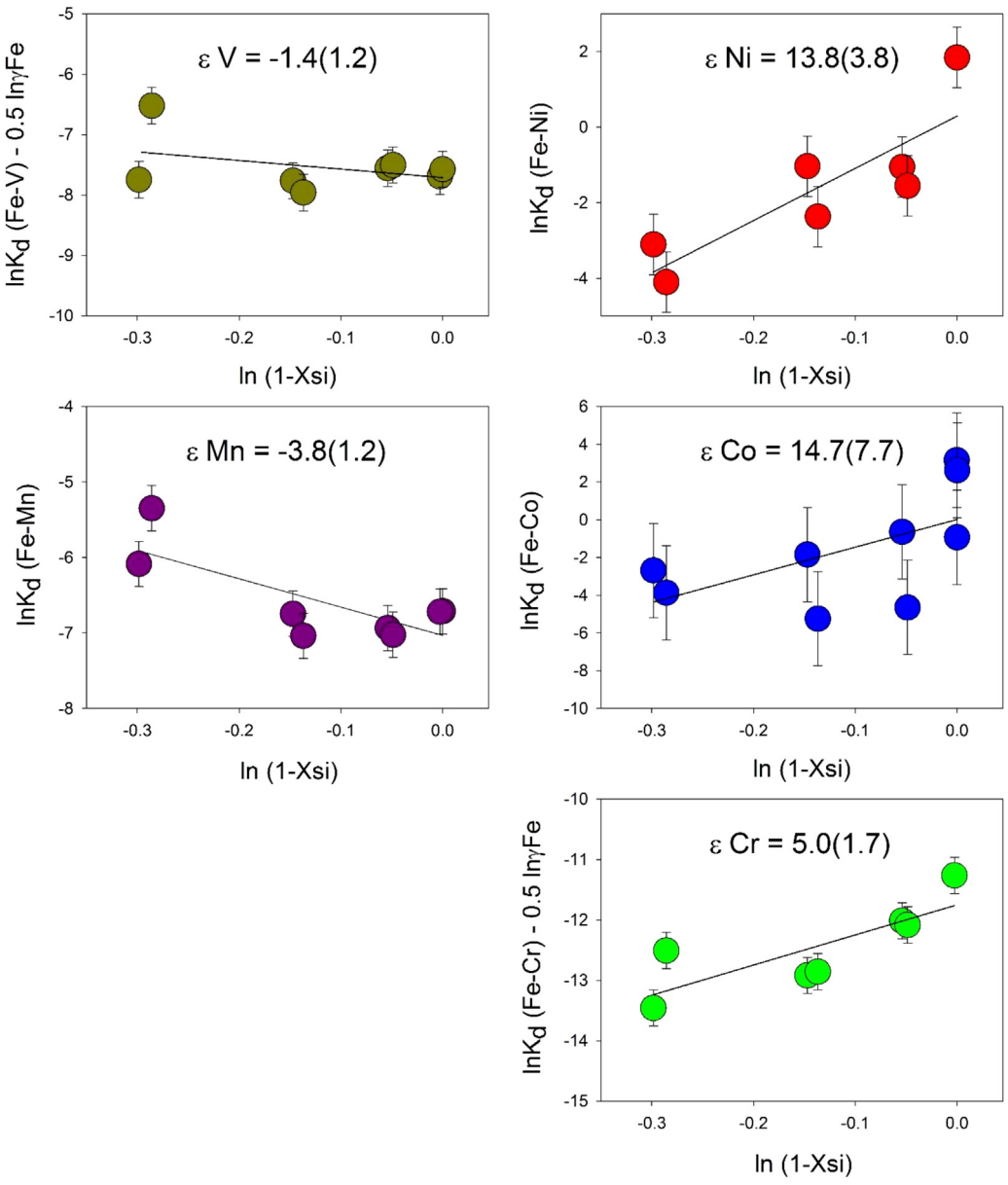

Fig. 4. $\ln K_d$(Fe-Ni), $\ln K_d$(Fe-Co), $\ln K_d$(Fe-Mn), $\ln K_d$(Fe-V), and $\ln K_d$(Fe-Cr) versus $\ln(1-X_{Si})$ from experiments across a wide range of Si contents in metallic Fe. The slope of the lines yields the interaction parameter for each – ε_{Ni}, ε_{Co}, ε_{Mn}, ε_{V}, and ε_{Cr} - in Fe-Si liquids.

(by weight) of siderophile element in the liquid silicate, $D^i_{SS/LS}$ is the partition coefficient (by weight) between solid silicate and liquid silicate, and $D^i_{LM/LS}$ (=$D(M)$ here) is the partition coefficient (by weight) between liquid metal and liquid silicate (Righter et al., 1997). For Earth calculations, $x = 0.68$, and $p = 0.6$, which reflects an intermediate depth magma ocean (e.g., Wood, 2008; Righter, 2011) and $D^i_{LM/LS}$ is calculated using:

$$\ln D'(M) = \ln D(M) + \ln \gamma(M)_{\text{met}} = a \ln fO_2 + b/T + cP/T + d(nbo/t) + e \quad (6)$$

and the regression coefficients (a through e) are given in Table 4. $D^i_{SS/LS}$ is <1 for all elements and specifically $D^{Zn} = 0.5$, $D^{Ga} = 0.3$, $D^{Cu} = 0.8$, $D^{Pb} = 0.01$, $D^{P} = 0.1$, $D^{Pd} = 0.1$, $D^{Au} = 0.1$, and $D^{Pt} = 0.05$, based on the studies of Davis et al. (2013), Sharp et al. (2015), Righter et al. (2015), Righter and Drake (2000), and Michely et al. (2017). The $\gamma(M)_{\text{met}}$ values are calculated as described in Section 4.6, with Ga, Au, Pd, Pt, and P activity coefficients using epsilon interaction parameters for high and low Si metal contents, as described in the Supplementary Information and presented in Figs. 7–11, and 14. As one might expect, Si content of the metal and fO_2 are related – in our calculations, changing fO_2 will change the Si content of the metal, and that will change the activity coefficient $\ln\gamma(M)$, so these connected parameters are all accounted for.

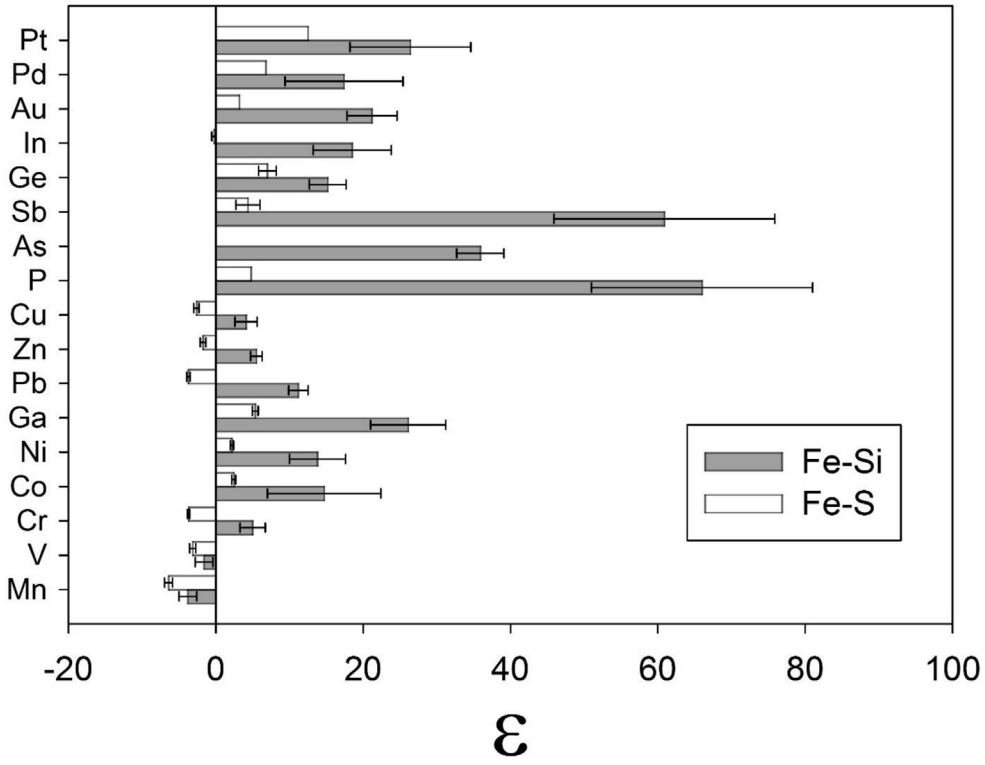

Fig. 5. Comparison of our new epsilon parameters for various elements in the Fe-Si liquids to those for Fe-S liquids measured in previous studies (Wood et al., 2014; Steelmaking Database, 1988). Also included are data for Fe-Si liquids reported by Righter et al. (2017) for Ge, In, As, and Sb.

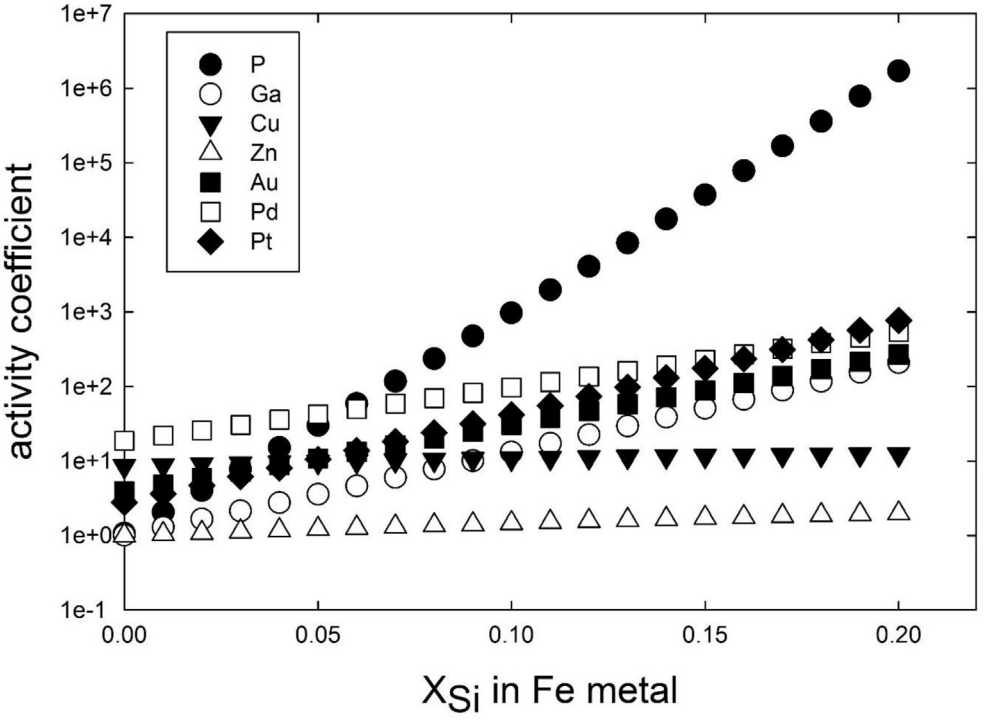

Fig. 6. Variation of activity coefficients for Au, Pd, Ga, Cu, Zn and P as X_{Si} increases, while temperature and pressure are constant at 1600 °C and 1 GPa, respectively. Note the strong effect of Si on the activity coefficient for P, as expected from its high epsilon interaction coefficient of 66 (Fig. 2).

Table 4
Regression coefficients for partitioning expressions[a]. $\ln D(M) = a\ln fO_2 + b/T + cP/T + d(nbo/t) + e - \ln\gamma(M)_{met}$ (Eq. (6)).

	P	1σ	Zn	1σ	Ga	1σ	Cu	1σ	Pb	1σ	Pd	1σ	Au	1σ	Pt	1σ
a	**−1.06**	*0.11*	**−0.76**	*0.06*	**−0.895**	*0.08*	**−0.083**	*0.061*	**−0.51**	*0.08*	**−0.18**	*0.02*	**−0.165**	*0.02*	**+0.19**	*0.02*
b	**−70621**	*6500*	**−48650**	*4500*	**−63068**	*2500*	**−5290**	*4600*	**−36263**	*5900*	**+29740**	*2900*	**+18345**	*1600*	**+31130**	*2700*
c	**2039**	*170*	**891**	*90*	**1024**	*63*	**−346**	*310*	**331**	*186*	**−9.28**	*5.61*	**20.5**	*9.9*	**−83.5**	*13.5*
d	**−1.23**	*0.19*	**0.16**	*0.09*	**−1.13**		**−0.35**	*0.24*	**+0.062**	*0.03*	**+0.43**	*0.24*	**−0.52**	*0.20*	**0.60**	*0.28*
e	**17.23**	*1.87*	**6.77**	*1.40*	**17.3**	*1.2*	**7.93**	*2.88*	**15.13**	*2.88*	**−5.63**	*1.96*	**−0.097**	*0.83*	**2.46**	*1.75*
n	**122**		**96**		**169**		**50**		**76**		**144**		**85**		**158**	
r^2	**0.82**		**0.81**		**0.77**		**0.88**		**0.78**		**0.81**		**0.93**		**0.88**	
2σ	**1.51**		**0.61**		**1.18**		**0.94**		**1.14**		**1.30**		**1.08**		**0.93**	

Bold indicates the coefficient value, and italics indicate 1 sigma error the coefficient.
[a] P, T, fO_2 range and references used in the regressions are summarized in Supplementary Information.

The regression results for partition coefficients for Au, Pd, Pt, P, Ga, Cu, Zn, and Pb are summarized in Table 4, and include additional partitioning data summarized in the Supplementary Information. The datasets used cover a very wide range of pressure, temperature, fO_2, and silicate melt compositions. In some experiments involving HSEs, HSEs are present in 3–5 wt% levels in the metal and have been corrected to infinite dilution in order to ensure that Henry's Law is obeyed (e.g., Mann et al. (2012) and; Righter et al. (2015). Although there is some uncertainty in the valence of siderophile elements under ultra-high pressure and temperature conditions, the values of the $\ln fO_2$ coefficient derived here are consistent with Au^{1+}, Pd^{1+}, Cu^{1+}, Zn^{2+}, Pb^{2+}, Ga^{3+}, and P^{5+} (Table 4); there is no evidence for a valence change for any of these elements (e.g., Corgne et al., 2008; Righter et al., 2010; Siebert et al., 2011). Platinum, on the other hand, perhaps expected to be 2+ or 4+ at terrestrial mantle conditions (FMQ), appears to undergo a valence change at fO_2 range relevant to core formation, such that Pt may be only weakly dependent upon fO_2. This behavior is suggested by the low and positive value of our 'a' regression coefficient here, but also from several previous independent studies (Medard et al., 2016, 2015; Bennett et al., 2016).

5.1.2. P-T-fO_2 during accretion of Earth – hot or cool magma ocean, reduced or oxidized?

There is some debate about the specific PT conditions of metal-silicate equilibrium, and whether the oxygen fugacity in the mantle changed during accretion or was relatively constant. First, studies of peridotite melting relations have revealed uncertainty in the liquidus temperatures – Fiquet et al. (2010) favor a hotter liquidus, while Andrault et al. (2011) favor a relatively cool liquidus. The differences in the melting curves are most pronounced at pressures greater than 20 GPa, and at 50 GPa the temperature difference is nearly 1000 K. These two different results have fundamental implications for the early thermal history and development of the mantle, and therefore it seems prudent to consider both scenarios to evaluate the resulting siderophile element concentrations for each. As a result, we carry out calculations along the PT conditions of the liquidus for both scenarios. Second, modelling suggests that fO_2 started low and eventually became higher during accretion (e.g., Wood et al., 2006; Rubie et al., 2011), whereas some recent calculations indicate that fO_2 may have decreased or changed only slightly during accretion (Righter and Ghiorso, 2012a,b; Siebert et al., 2013, respectively). Therefore, two accretion models are considered for Earth – relatively constant fO_2 and increasing fO_2 - and include the evolving S, C, Si content of the core (Fig. 7b), and FeO content of the mantle ($X_{FeO} = 0.01–0.06$) as accretion proceeds (Fig. 7a). For these scenarios, the core metallic liquid S, C, and Si composition is calculated according to the metal-silicate partitioning studies of Siebert et al. (2013), Boujibar et al. (2014), and Chi et al. (2014), respectively. The compositional variation also causes orders of magnitude change in the activity coefficient of the trace SE (Fig. 7c). And finally, we consider metallic liquids that are Si-bearing and Si-free, to illustrate the specific effect of Si on the partitioning.

5.1.3. Investigation of PT gradient, fO_2 and Si content

When the activity variations are combined with pressure, temperature, fO_2, and melt compositional effects (Eq. (6)), the mantle abundances of these elements resulting from metal-silicate equilibrium can be calculated in several scenarios for the deep molten early Earth (Eq. (5)). For, P, Ga, Zn, Cu, and Pb, it is possible to explain Earth's mantle abundances of these elements by metal-silicate equilibrium near 50 GPa, 3800 K, with variable fO_2, and a Si-rich core (10% Si, 2% S and 1% C). Such a scenario with a Si-bearing core is consistent with moderately siderophile refractory elements Ni, Co, Mo, and W (e.g., Siebert et al., 2011), that also suggest a core-mantle differentiation at high pressure with Si as a dominant light element (Tuff et al., 2011; Righter et al., 2016). At those conditions, Au, Pd and Pt, on the other hand, become higher than observed in Earth's mantle. They require a process that removes them from the mantle, such as a sulfide-rich Hadean matte (see Section 5.1.4). The sensitivity of these results to liquidus temperature, redox path, and metallic liquid composition are discussed separately below.

5.1.3.1. Hot vs. cool magma ocean. Pt, P, Ga, and Zn are not sensitive to temperature differences in the metal-silicate equilibrium and are easily explained by either the hot or cool scenario (calculated along variable fO_2 curves in Figs. 8a, 9a, and 11a). Cu and Pb exhibit some dependency on temperature and shows a closer match to PUM values at the hotter conditions of the Fiquet et al. (2010) melting curve. Au and Pd show significant temperature dependence

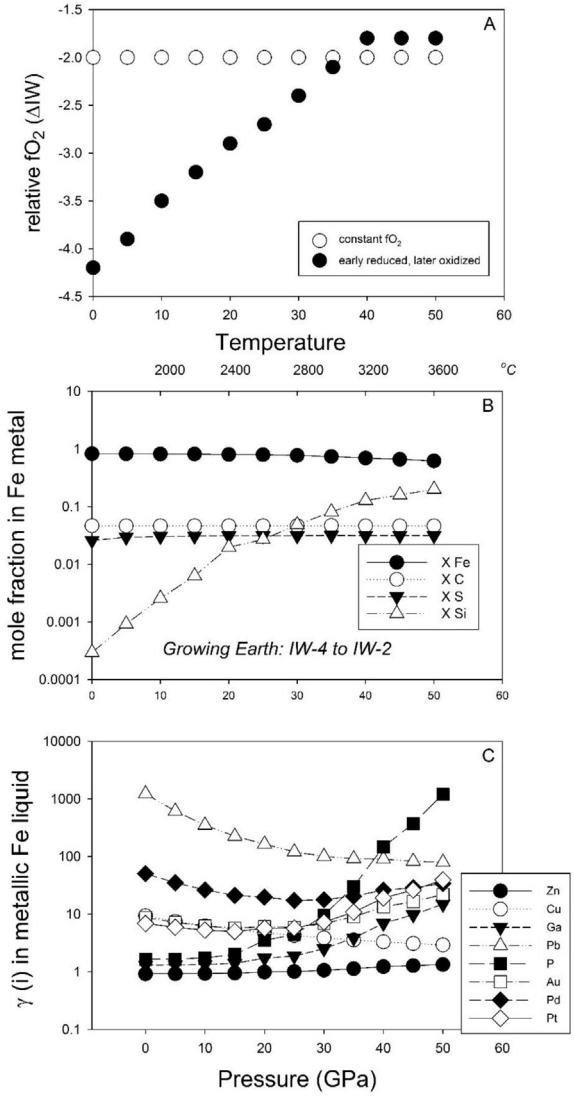

Fig. 7. (A) Variation of fO_2 with pressure during accretion, for the two models considered here; one has constant relative fO_2 at IW-2, whereas the other has fO_2 increasing during accretion, starting near IW-4, and ending just above IW-2. (B) Variation of X_S, X_C, X_{Si}, and X_{Fe} in metallic liquid as accretion proceeds and pressure increases for the scenario where oxygen fugacity starts near IW-4 and increases during accretion to IW-2 (Fig. 7A). (C) Variation of activity coefficients for Au, Pd, Pb, Ga, Cu, Zn and P as accretion proceeds along the fO_2 path (starts reduced (IW-4) and ends more oxidized (IW-2)) and compositional change (mainly that Fe metallic liquid becomes more Si-rich) shown in Fig. 7B.

which means that the cooler liquidus of Andrault et al. (2011) favors a match to PUM values at higher pressures than the hotter liquidus of Fiquet et al. (2010) (Figs. 10a and 11a).

5.1.3.2. Variable vs. constant fO_2. Zn, Au, Pd and Pt, all with low valence in silicate melt, are not sensitive to fO_2 differences in the metal-silicate equilibrium and PUM values are easily attained in either the variable or constant fO_2 scenarios (calculated along the hotter PT gradient in Figs. 8b, 10b, and 11b). Cu and Pb exhibit some dependency on fO_2 and show a closer match to PUM values at the variable fO_2 conditions (Fig. 10b). P and Ga show significant dependence on fO_2 which means that the reduced to oxidized accretion path leads to a match to PUM values at high pressures of 35–50 GPa (Figs. 8b and 9b). In comparison, the constant fO_2 accretion scenario leads to much lower Pb and P abundances, and higher Ga abundances in the PUM (Figs. 8b, 9b, and 10b).

5.1.3.3. Effect of Si in the core. The final variable to explore is the effect of Si specifically. We calculate mantle concentrations for all elements along the hotter PT gradient and for the variable fO_2 accretion scenario, where one case contains Si, S, and C alloyed in the metal and the other only S and C. Zn and Cu, both with small positive interaction parameters with FeSi liquids are not especially sensitive to X_{Si} in the core forming metallic liquid; PUM values are easily explained in either the Si-S-C or S-C metallic liquids scenario (calculated along the hotter PT gradient in Figs. 8c and 9c). Au, Pd, and Pt, all with moderately high and positive interaction parameters with FeSi liquid, are slightly more sensitive to X_{Si} in the core forming metallic liquid. PUM values of Au, Pd and Pt are attained at even lower pressures easily explained in either the Si-S-C or S-C metallic liquids scenario (calculated along the hotter PT gradient in Figs. 10c and 11c); in fact, the concentrations become too high at the 35–50 GPa range where other elements are easily explained. This overabundance will be addressed in Section 5.1.4. Pb exhibits some dependency on X_{Si} in the core forming metallic liquid and shows a closer match to PUM values when a Si-bearing metallic liquid is involved (Fig. 10c). P and Ga show the most significant dependence on X_{Si}. The calculations with Si-bearing metallic liquids lead to a good match to PUM values whereas the Si-free metallic liquid scenario leads to Ga and P abundances in the PUM that are too low by several orders of magnitude (Figs. 8c and 9c). Specifically, the Si-free metallic liquid scenario leads to higher D(Ga) and D(P) and demonstrates that high Si core forming metal is required to explain the depletions of Ga and P. The role of Si is at face value counter-intuitive – one might expect a lower fO_2 to cause a much higher D value. But, because dissolved Si in Fe causes avoidance of so many trace siderophile elements (Ge, In, As, Sb from Righter et al., 2017; Ga, P, Cu, Zn, Pb – this study) the metal/silicate Ds. at lower fO_2 stay low, and metal-silicate equilibration produces elevated trace siderophile element concentrations in the silicate (or the mantle in the case of our modelling).

5.1.3.4. Summary. The HSE examined here – Au, Pd, and Pt – all become overabundant in the primitive upper mantle in the scenario of core-mantle equilibration during accretion. Recall that Righter et al. (2008) argued the Pd could be explained by a deep metal-silicate equilibrium. Although this conclusion is still valid for Pd alone, an explanation for Au, Pd, and Pt combined requires slightly lower PT conditions than those required of ~15 other MSE and WSE (Ni, Co, Mo, W, P, Ga, Ge, Cu, Sn, Sb, As, In, Mn, V, Cr; e.g., Righter, 2011; Wade et al., 2012; Righter et al., 2017; this

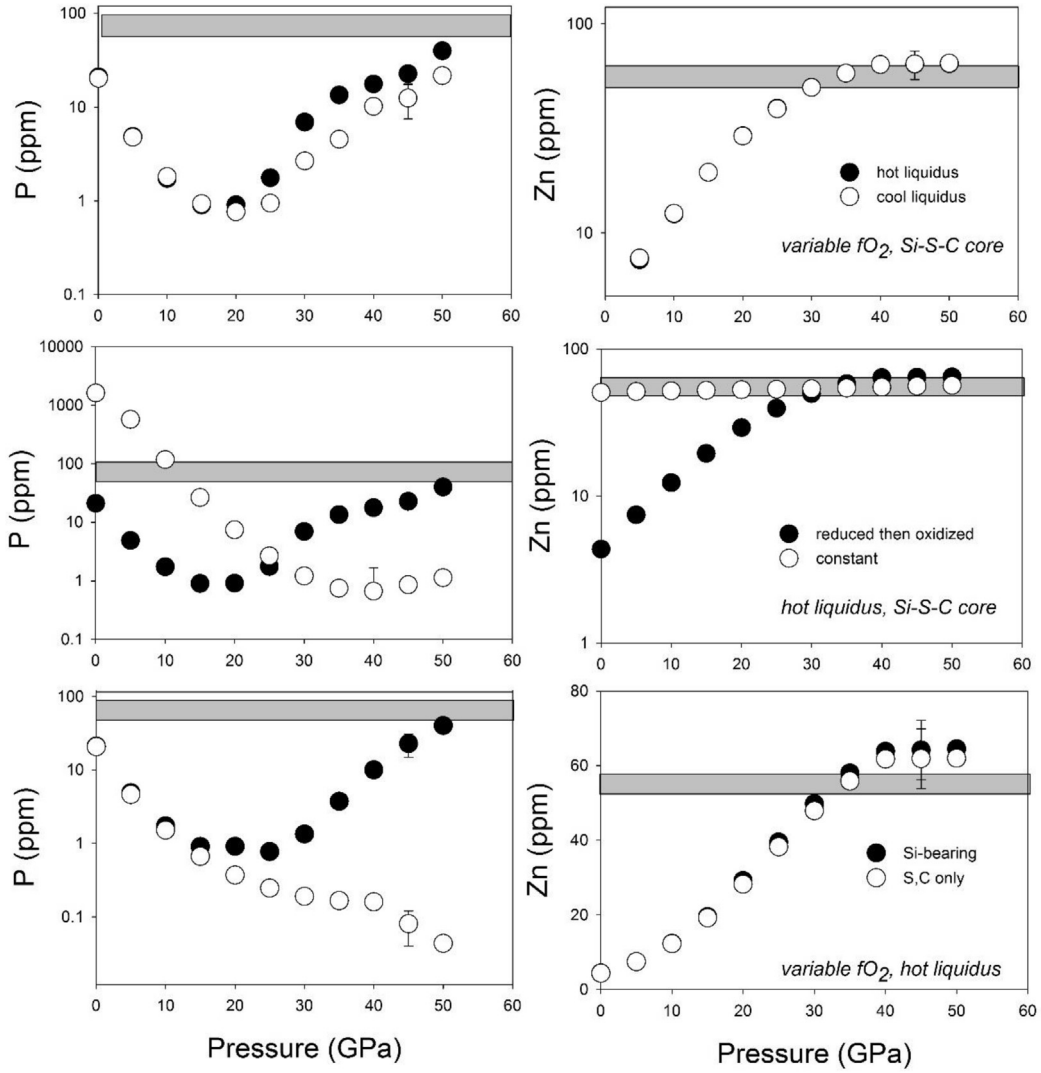

Fig. 8. Variation of P and Zn concentrations in an evolving magma ocean as accretion proceeds, with attention to three different variables – temperature, fO_2, and Si content of the metal. The top two diagrams illustrate the effect of temperature, with one path calculated for a hotter liquidus after the phase equilibria of Fiquet et al. (2010), and a cooler liquidus after Andrault et al. (2011) (both using an fO_2 path of reduced to oxidized). The middle two diagrams show the effect of two different fO_2 paths during accretion – one in which fO_2 is constant and the other for fO_2 changing from near IW-4 to IW-2 (both using hotter gradient). The bottom two diagrams show the specific effect of including effects of Si in the FeNi metallic liquid on the modelling; one case includes Si. S and C, and the other case excludes Si and only includes the effect of S and C (both use the hotter gradient). Horizontal shaded regions are primitive mantle estimates (Palme and O'Neill, 2014).

study), and indicates the difficulty of explaining the MSE, WSE and HSE mantle abundances in a single set of conditions or single accretion pathway. Instead the HSE require multi-stage processes that will be explained below.

5.1.4. Post core formation processes

The overabundance of Au, Pd, and Pt in the mantle predicted by the metal-silicate equilibrium modelling above causes a problem that is the opposite to that previously and traditionally argued in which the mantle is stripped of HSEs due to the $D_{HSE} > 1000$ during metal-silicate equilibrium (e.g., Chou, 1978; Holzheid et al., 2000; Mann et al., 2012; Brenan and McDonough, 2009). In this traditional hypothesis, the near chondritic relative HSE contents are produced by the addition of a late veneer after core formation. Problems with this overall concept were noted by Righter et al. (2008, 2015), Wheeler et al. (2011), and Bennett et al. (2016) all of whom showed that Au and Pd contents of the PUM could quite easily be attained or even exceeded by metal-silicate equilibrium at high PT conditions. The new results reported here for Fe-Si alloys exacerbate the problem. This overabundance may obviate the need for standard late veneer addition to achieve PUM HSE levels, and instead requires the opposite – a removal mechanism. Here we consider two post core formation mechanisms that may have lowered the HSE content of the BSE as a deep magma ocean crystallizes – a late reduction, and a late sulfide matte. The late veneer is also

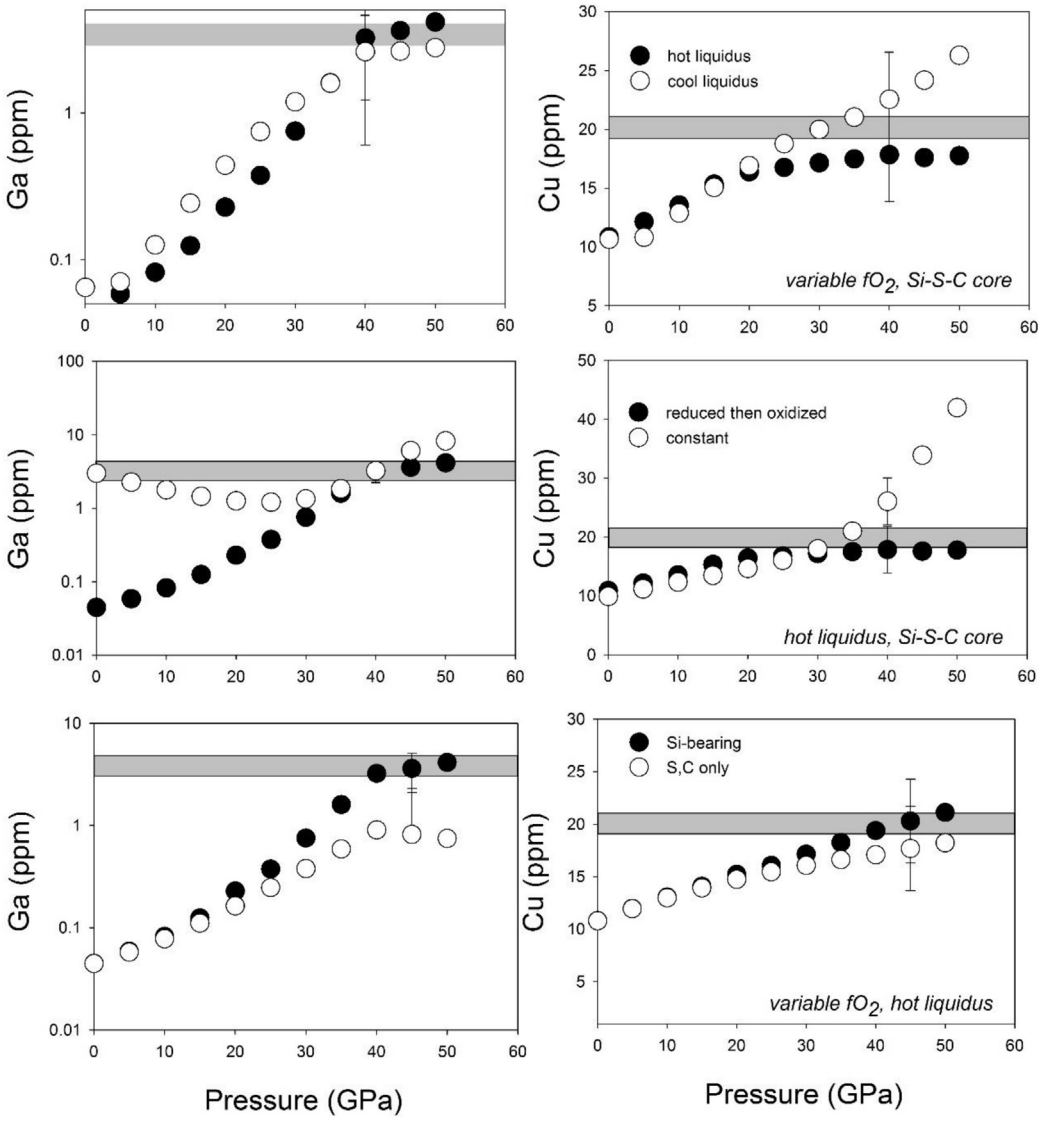

Fig. 9. Variation of Ga and Cu in Earth's silicate mantle as accretion proceeds, for the same three examples of variable temperature, fO_2, and metallic liquid composition described in Fig. 8.

discussed as a way to augment the HSE content of the mantle and establish the chondritic relative concentrations of the 8 HSE.

5.1.4.1. Late reduction in a shallow magma ocean. Because Au, Pd, and Pt contents of Earth's mantle may have been quite high after formation of a deep magma ocean, there must be a mechanism to remove HSEs from the mantle. Here we consider two possibilities: late reduction caused by accretion of reduced material, or reduction caused by isolation of the mantle from the atmosphere by a protocrust. Because a late veneer may have been metal-bearing material like EH chondrites (Burkhardt et al., 2011), it is natural to consider what if a metal-bearing late veneer was added during the crystallization of a magma ocean? A metal-bearing late veneer could be an HSE removal mechanism because the addition of metal that gets intimately mixed into and equilibrated with the magma ocean would concentrate HSEs and remove them as metal ultimately sunk to the base of the magma ocean. As crystallization progresses from the bottom up (Solomotov, 2007), the magma ocean would become shallower and any metal precipitated from or added to the mantle would be Si-poor relative to the deeper core forming metal. Thus, the D(Au), D(Pd), and D(Pt) metal/silicate would be higher than during the deep magma ocean event and be able to remove Au, Pd and Pt from the mantle.

A second possibility is that after formation of Earth's protocruast and isolation of the mantle from the atmosphere, there may have been volcanic outgassing that could have caused reduction of the mantle. Because the mantle was reducing early in this stage of Earth's history, not much reduction would be necessary to stabilize a small amount of metal that could serve as a host phase for HSE and remove them to the base of the mantle.

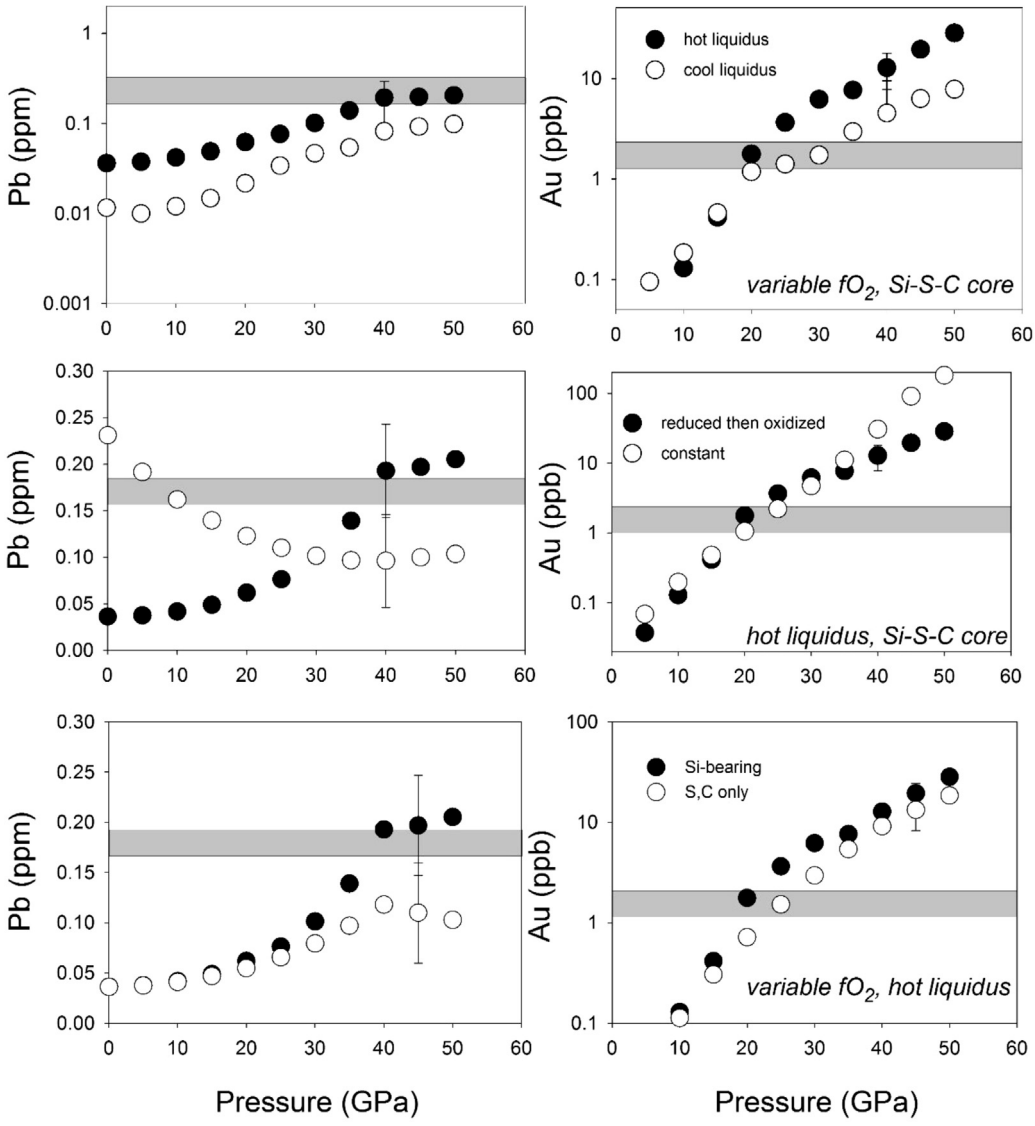

Fig. 10. Variation of Pb, Au and Pd in Earth's silicate mantle as accretion proceeds, for the same three examples of variable temperature, fO_2, and metallic liquid composition described in Fig. 8.

We consider a scenario where a deep magma ocean crystallizes from 50 GPa to depth of 20 GPa (~80% crystallization), and then either a metal-bearing late veneer is added, or a small amount of metal is stabilized during a reduction process during degassing. With a metal-silicate segregation event and involving only a small fraction of metal (0.005 mass fraction; Fig. 12), this would be one way of removing HSEs from the mantle, while not affecting MSE such as Ni, Co, and W. This idea is perhaps consistent with the Marchi et al. (2018) concept of a late impactor population affecting Earth, but instead of adding HSE's it removes them because the veneer contains a small amount of metal that segregates to the bottom of the molten mantle. If this late veneer material is like E chondrites it will have O, Ru and Mo isotopic characteristics like Earth (Fischer-Gödde and Kleine, 2017). One challenge for this scenario might be how to efficiently segregate a small amount of metal through to the base of the magma ocean, but otherwise it could quantitively explain the mantle Au, Pd and Pt content (Fig. 12).

5.1.4.2. Late sulfide matte. Another concept that allows removal of HSEs and chalcophile elements from the mantle is that of a late Hadean sulfide matte (e.g., O'Neill, 1991; Ballhaus et al., 2017). Because sulfide liquids have a strong affinity for HSEs and other chalcophile elements, they could be called upon to remove these elements from the mantle, and some argue that such a sulfide segregation would have established the Sn and Pb contents of Earth's mantle, for example (Ballhaus et al., 2017). For this mechanism to work, sulfide saturation must occur at the conditions relevant to an evolving magma ocean. Sulfide liquid will stabilize in a magma ocean when the silicate melt attains the saturation limit with respect to S, or the sulfur

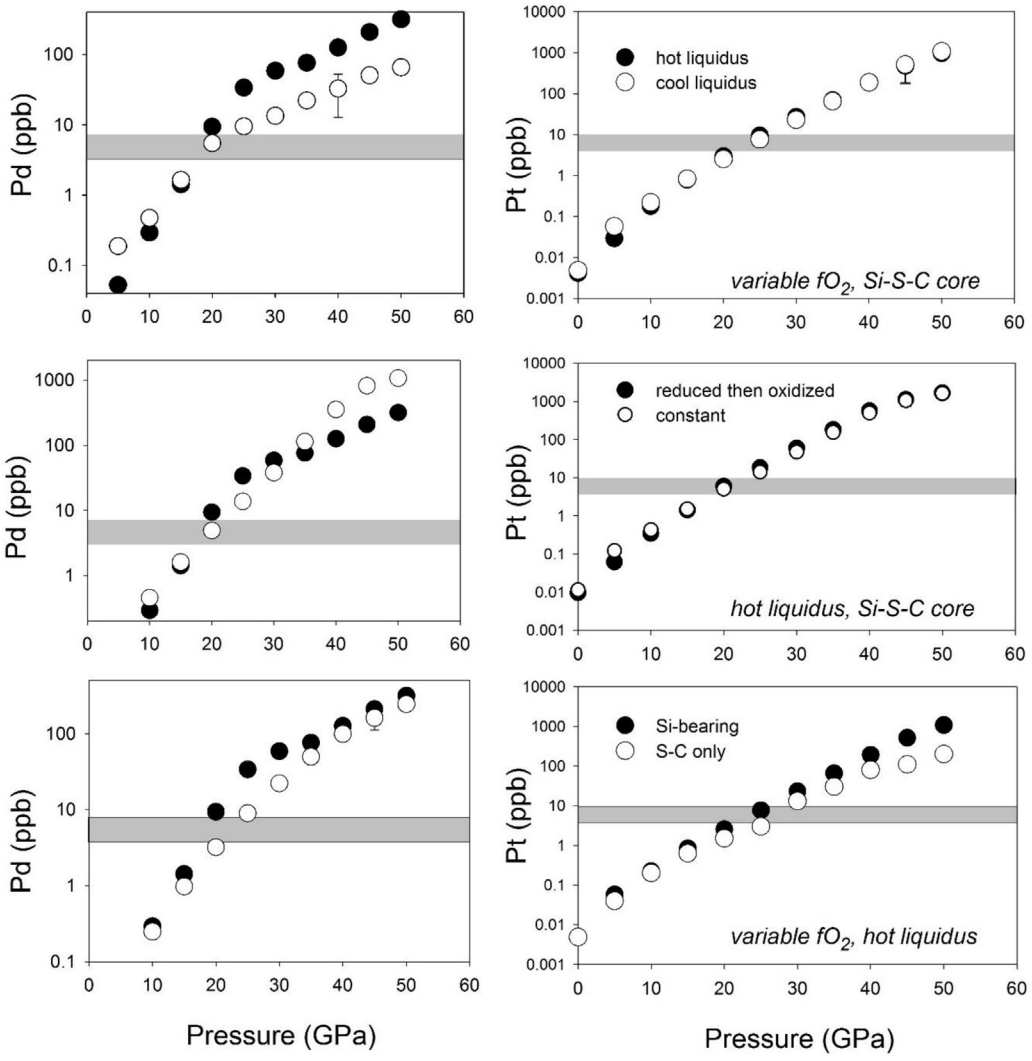

Fig. 11. Variation of Pd and Pt in Earth's silicate mantle as accretion proceeds, for the same three examples of variable temperature, fO_2, and metallic liquid composition described in Fig. 8.

content at sulfide saturation (SCSS). The SCSS is known to be pressure dependent with the solubility of S decreasing SCSS at higher pressure, and of course is highly studied and relevant to the stability of sulfides at crustal magmatic conditions where sulfide can crystallize from basic melts (e.g., Haughton et al., 1974; Holzheid and Grove, 2002; Righter et al., 2009; Ding et al., 2014). Because of this, a magma that is saturated with sulfide at high pressure, will become immediately undersaturated as it rises to shallower depths. As a result, a magma may be saturated with sulfide at great depth, but undersaturated at shallower depths until there has been sufficient silicate crystallization to drive the S contents to higher values. To apply this concept to a terrestrial magma ocean, we must have an understanding of the SCSS for a peridotite magma ocean. Studies on peridotite liquids of Li and Agee (2001), Boujibar et al. (2014), and Laurenz et al. (2016) across a wide range of pressures, can be used to estimate the SCSS for peridotite melts. Consideration of these studies shows that S contents for SCSS are near 1000 ppm at PT range of ~25 GPa and 2400 °C, and increase to 4000–6000 at the lower PT range of ~3 GPa and 1800 °C (Fig. 13). The implication for the early Earth is thus that the SCSS will be very low at high pressure conditions, but once magma ascends it will become immediately sulfide-undersaturated at shallower conditions. A convecting magma ocean will thus experience cyclical saturation and under saturation as a S-bearing packet of magma ascends and descends in a convective cell, and sulfide saturation – if it occurs – will be at the deeper portion of the magma ocean.

Whether an early magma ocean will saturate with sulfide at all depends on how much S is present after core formation. If S-bearing core-forming metal equilibrated with a magma ocean at high pressures, as advocated by many (e.g., Righter et al., 1997; Wade and Wood, 2005; Righter, 2011; Rubie et al., 2011; Labidi et al., 2013; Suer et al., 2017), $D(S)$ metal/silicate will vary from ~10 to 250, producing increasingly S depleted magma ocean with

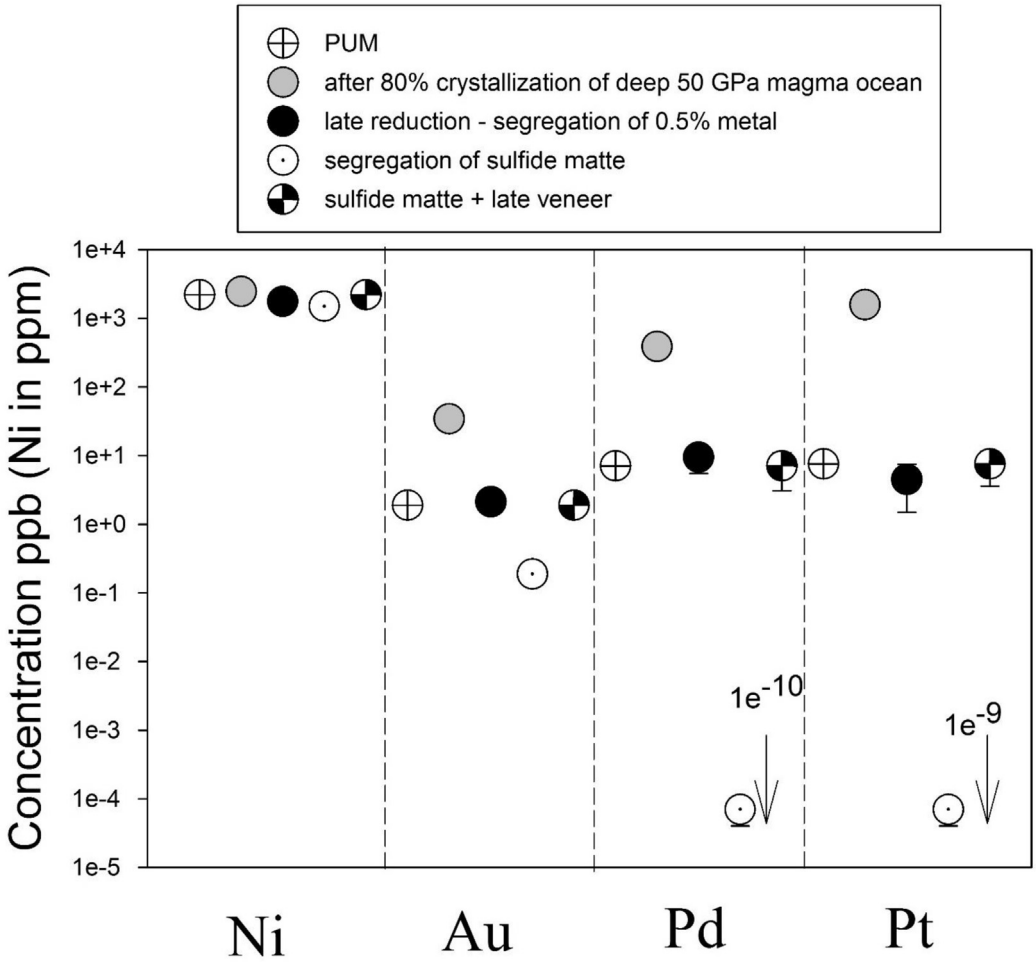

Fig. 12. effect of segregation of small amount of metal after late veneer addition into shallow magma ocean (20 GPa). Ni, Au, Pd and Pt concentration in the primitive upper mantle (PUM; circles with cross) compared to those calculated after core formation at the end of accretion where metal silicate equilibrium is achieved near 50 GPa and 3600 K followed by 80% crystallization (~20 GPa) of the magma ocean (gray circles). Solid circles are calculated Ni, Au, Pd, Pt concentrations after late reduction with segregation of a metal mass fraction of 0.5% that removes more HSE. Open circles with a dot are the resulting mantle concentrations after segregation of a late sulfide matte (using sulfide/silicate partition coefficients of Mungall and Brenan, 2014 and as shown in Fig. 14a). And checkered symbols represent the mantle concentrations resulting from the late sulfide matte, followed by addition of a late oxidized veneer. Partition coefficients for the late reduction for Au, Pd, Pt, are calculated using Righter et al. (2015) for 20 GPa, 2400 °C, IW-2, $nbo/t = 2.5$, and are D(Au) = 4000, D(Pd) = 8000, and D(Pt) = 70000. D(Ni) = 80 are calculated for the same conditions. Bulk mantle partition coefficients (solid/liquid silicate) for the crystallization of the magma ocean are 0.5, 0.1, 0.1, and 0.05 for Ni, Au, Pd, and Pt, respectively.

increasing depth (Fig. 13). In fact at all pressures, the S content of a magma ocean will be lower than the SCSS (e.g., 650 ppm at 50 GPa). It will only be possible to drive magma ocean S contents high enough for saturation in a deep magma ocean after a significant amount (~50%) of crystallization of the magma ocean (~30 GPa – gray symbols in Fig. 13), for two reasons. First, because S is incompatible in deep mantle silicates it would be increased in the melt during crystallization. Second, the temperature drops that would accompany crystallization (~100 °C at ~3–5 GPa, and ~250 °C at 40–50 GPa, according to the liquidus and solidus relations of Andrault et al., 2011), would cause the SCSS to drop to lower values (Fig. 13). However, even so, once sulfide is removed from the system, the S content of the magma ocean is decreased overall and would require even more crystallization (and temperature drop) to saturate again. This process would have a limited lifetime and could only support a small amount of sulfide saturation before the supply of S would become too low to reach SCSS.

Given these constraints and challenges, and assuming that there is a way to crystallize a deep magma ocean by 50% and thus to saturate sulfide at its base, we can calculate the effect on the HSE contents. We use two sets of D(Au), D(Pd), and D(Pt) sulfide/silicate liquid partition coefficients to illustrate the range of outcomes with the existing partitioning data - Mungall and Brenan (2014) determined at 1 GPa and Laurenz et al. (2016) determined at 11 GPa. Use of either set of partition coefficients shows that it is possible to lower Au, Pd, and Pt concentrations with

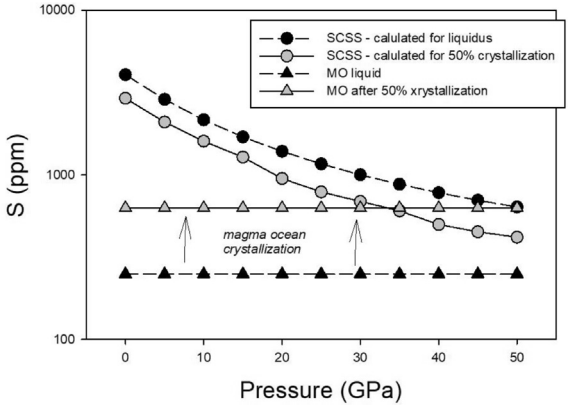

Fig. 13. Curves of the SCSS calculated using Eq. (1) from Rubie et al. (2016), for PT path of liquidus and ~50% crystallized (approximated by $T_{solidus} + (T_{liquidus} - T_{solidus})/2$ using phase equilibria of Andrault et al., 2011). Solid circles are for liquidus temperatures and shaded circles are for 50% crystallization (again, approximated by $T_{solidus} + (T_{liquidus} - T_{solidus})/2$ using phase equilibria of Andrault et al., 2011). S content of post core formation magma ocean (MO; 100% molten = black triangles and 50% crystallized = gray triangles) shown for comparison to SCSS. Dashed lines connect the fully liquid SCSS and MO, while solid lines connect the 50% crystallized SCSS and MO. Fully molten magma ocean will have S contents too low for sulfide liquid saturation (solid symbol curves never cross), but as the magma ocean starts to crystallize (arrows indicate increasing S contents during crystallization), the S contents exceed that of saturation and sulfide liquid saturation is possible at the deepest portion of a magma ocean (at pressures deeper than the intersection point of the shaded symbols). Sulfide liquids will not saturate under any reasonable conditions at shallower than 15–20 GPa, because the SCSS is higher than 1000 ppm.

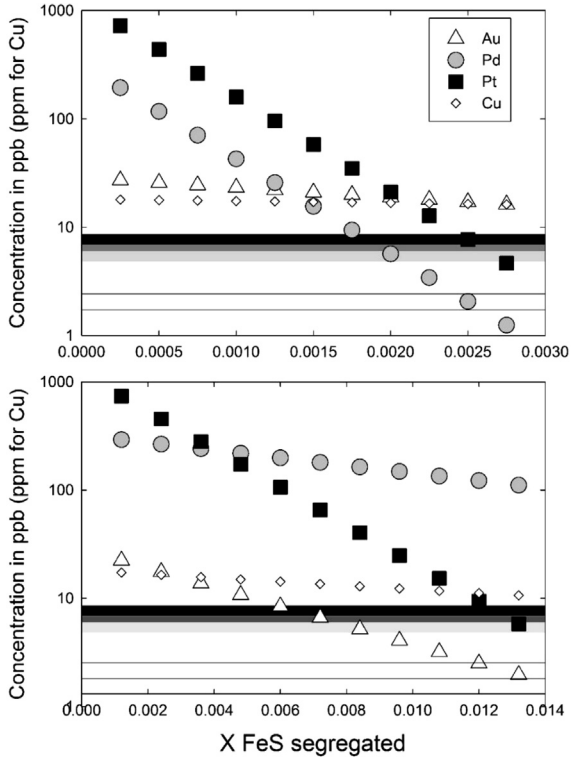

Fig. 14. Effect of sulfide liquid fractionation on concentrations of the highly chalcophile elements Au (white symbols), Pd (gray symbols), and Pt (black symbols), and the moderately chalcophile element Cu (small diamonds). Horizontal shaded lines are BSE mantle concentrations of the HSE – Au – white, Pd – gray, and Pt – black. Top diagram uses the sulfide liquid/silicate liquid partition coefficients of Mungall and Brenan (2014) determined at 1 bar and 1200 °C (D(Pd) = 4000, D(Pt) = 2×10^4; with D(Au) = 10^4 as per Mungall and Brenan (2014) since Au was not studied by Laurenz et al., 2016). The bottom diagram uses the sulfide liquid/silicate liquid partition coefficients of Laurenz et al. (2016) determined at 11 GPa and 2200 °C (D(Pd) and D(Pt) = 10^5; D(Au) = 10^4). Use of the 1 bar data shows that Pd and Pt are lowered to values near BSE values with segregation of from 0.2 to 0.3% sulfide from the mantle, but Au remains too high because of its lower sulfide/silicate D. Use of the 11 GPa data shows that Au and Pt are lowered to BSE levels with segregation of ~1.0% sulfide from the mantle, but Pd remains too high due to its lower value in the Laurenz et al. (2016) dataset. The other chalcophile elements such as Ni and Bi and Cu (shown) are largely unaffected by sulfide liquid fractionation due to their smaller sulfide/silicate partition coefficients relative to the HSE (see text for more discussion).

segregation of ~0.2–1.0% sulfide from the magma ocean (Fig. 14). If Mungall and Brenan (2014) values are used, it is possible to lower Pd and Pt to approximately BSE values with 0.2% sulfide, but the Au values remain high due to the lower D(Au) sulfide/silicate melt values. If the Laurenz et al. (2016) Pd and Pt values are used (and Au of Mungall and Brenan since Laurenz did not include Au), it is possible to lower Au and Pt values to approximately BSE values with ~1.0% sulfide, but the Pd values remain too high due to the lower D(Pd) than D(Pt) measured by Laurenz et al. (2016). If sulfide segregation is responsible for removing the excess of HSE from the PUM, then the sulfide will also affect the chalcophile elements Bi and Cu (which have D near 1000), but these are only minimally affected due to the small amount of sulfide involved (see the example of Cu in Fig. 14). For other chalcophile elements Ag, Pb, Co, As, Mo, Zn, Sn, Sb, Cd, In, Mn, Cr, all of which have D(sulfide liquid/silicate liquid) < 100 (Kiseeva and Wood, 2013; Li and Audetat, 2015; Hart and Gaetani, 2016), a late sulfide matte of this fraction would not significantly change the concentrations in the magma ocean, and so these elements are not sensitive indicators of a matte despite their chalcophility.

In summary, the late sulfide matte hypothesis is a potentially important way to remove HSE from the mantle, but the resulting pattern is unlikely to have chondritic relative HSE abundances. One must keep in mind that this hypothesis is only viable at the deepest pressures of the magma ocean due to the pressure dependence of the SCSS and initial magma ocean S content. Sulfide/silicate liquid partition coefficients have only been measured at relatively low pressures - there may be a pressure effect on HSE partitioning that should be examined in future studies.

5.1.4.3. Sulfide matte plus late veneer? We have seen that segregation of a late sulfide matte can remove either Pd and Pt, but not Au (or Pt and Au, but not Pd) to chondritic relative values, but not all three together. The higher Au,

(or Pd) in either scenario would require several % of sulfide removal, which would remove almost all of the other two elements. In other words, more HSE would have to be added to bring the levels to the high and chondritic relative concentrations again. So, in such scenarios, HSE need to be added to the mantle, and an easy way to do this is through addition of a standard late veneer (e.g. Rubie et al., 2016; Righter et al., 2016b).

The concept of a late veneer originated in the 1970 s when measurements of HSE in mantle materials showed high and chondritic relative abundances that could be explained by addition of chondritic material to the mantle after the core had formed (Kimura et al., 1974; Chou, 1978). The late veneer concept expanded to be the source of volatiles for Earth, coming in later and after a relatively volatile-poor or volatile –free accretion process (e.g., Chou et al., 1983; Morgan, 1986; Wang and Becker, 2013). Support for the late veneer has partially eroded as studies have shown that metal/silicate partition coefficients for HSEs are decreased substantially at the high PT conditions of core formation (e.g., Righter et al., 2008; Mann et al., 2012), sulfur isotopes suggest that S in Earth's mantle partially equilibrated with metal (Labidi et al., 2013), Pd-Ag isotopes indicate that Ag was added to Earth's mantle in the later stages of core formation (Schönbächler et al., 2010), and Earth's Mo and Ru isotopic compositions do not reflect additions from volatile-rich or carbonaceous chondrite-like material, but instead are akin to reduced and volatile-poor materials like E chondrites (Dauphas et al., 2004; Burkhardt et al., 2011). While the late veneer may only represent a fraction of the Earth's HSEs and volatiles, and certainly not the end member it once was thought to be, it must nonetheless be a consideration in explaining aspects of HSEs and volatiles.

If a late sulfide matte removed Au, Pd and Pt to lower than BSE values, addition of a late veneer could increase them again to the near chondritic relative levels observed in the PUM. Addition of $\sim 0.7\%$ of Earth's mass of chondritic material would allow this to happen. This last scenario then, the Earth's concentration of Au, Pd, and Pt would require a multi-stage process of core-mantle equilibrium, removal of a late sulfide matte, followed by addition of a late veneer (Fig. 12).

6. SUMMARY AND FUTURE WORK

The epsilon interaction parameters for Au, Pd, Pt, Ga, Cu, Zn, P, Pb, Ni, Co, Mn, and V have all been determined for FeSi alloys at 1600 °C and 1 GPa. These new values indicate that Si has a very large effect on the activity coefficients of Au, Pd, Pt, Ga, P, and a relatively small effect on Cu, Zn, and Pb. Our values for Ni, Co, Mn and V are in agreement with previous work. We present an updated epsilon interaction parameter model that can calculate activity coefficients for 31 trace siderophile elements in the Fe-S-C-Si system.

Ga, Cu, Zn, P, and Pb concentrations in Earth's primitive upper mantle can all be explained by metal-silicate equilibrium at the base of a deep (40–60 GPa) magma ocean during accretion. The specific effect of Si alloyed in the core is important and calculations that include only S and C (and no Si) yield P, Ga, and Pb concentrations lower than measured in Earth's primitive mantle. The final core composition in the variable fO_2 model is 10.2% Si, 2% S, and 1.1% C (or $X_{Si} = 0.18$, $X_S = 0.03$, and $X_C = 0.04$); consistent with As, Sb, Ge, and In (Righter et al., 2017), and also with moderately siderophile Ni, Co, Mo and W.

Concentrations of Au, Pd and Pt, on the other hand, become too high at these conditions and require a removal mechanism such as reduction involving segregation of metal to the base of the magma ocean (accretion of reduced material, or an indigenous process), or segregation of a late sulfide matte. A late reduction event can effectively remove HSE to levels close to those in the PUM, but would require that such a small fraction of metal can efficiently segregate through the mantle. Separation of a sulfide matte at the base of a deep magma ocean is possible as long as the magma ocean crystallizes to at least 50% and the extent of sulfide segregation is ~0.2–1.0%. Any sulfide matte model must also be consistent with the chalcophile elements Ni, Cu, and Bi, whose concentrations will also decrease with the segregation of such a matte. However, we show that sulfide segregation would leave the mantle with low and non-chondritic ratios of Au, Pd, and Pt. An explanation for the near chondritic relative ratios of the HSE could be provided by a combination of sulfide matte plus late veneer – ultimately a three stage process.

Mn and P, two siderophile elements that are central to biochemical processes (photosynthesis and tri-phosphates, respectively), have significant and opposite interactions with FeSi liquids, and whose mantle concentrations would be notably different with a Si-free core.

These results suggest that accretion and core formation (involving a Si, S, and C-bearing metallic liquid) were the dominant processes establishing the HSE and volatile contents of the terrestrial mantle. Late reduction or separation of a sulfide matte (indigenous) combined with a late veneer (exogenous) were possible secondary, but nonetheless important processes establishing Earth's mantle HSE concentrations. The viability of these scenarios and conclusions could be tested several ways.

First, experimental data for O-bearing FeNi liquids are needed to augment modelling for Earth or Mars where some O solubility may occur – this would be a valuable goal of future studies. We have some general impression of how O might affect elements, but they may be misleading and deserve further study. For example, the results of Chabot et al. (2015) for effect of O on some elements in metallic solid–liquid systems are in agreement with measurements in metal/silicate systems (e.g., Ag, Mn, V and Cr all become more siderophile in Fe-O liquids). However, there are also discrepancies that cannot be explained - Blanchard et al. (2015) demonstrate Ga becoming more siderophile with O alloyed in the metal, while Chabot et al. (2015) show Ga behaving indifferently to O content. Similarly, Wade and Wood (2005) utilize negative epsilon interaction parameter for Sn, As and Sb in Fe-O liquids, but Chabot et al. (2015) report O avoidance (or positive epsilon interaction parameter) for all three. So, the use of solid metal –liquid metal experiments as a guide to metal-silicate systems should be used very cautiously.

Second, the activity coefficients are based on interaction coefficients determined at relatively low pressures (1 bar to 1 GPa). Pressure effects of the interaction coefficients might be small, but are not currently accounted for. Future efforts might focus on isolating any pressure effects on activity (e.g., Steenstra et al., 2017).

Third, the metal-silicate and sulfide/silicate partition coefficients utilized in the regression analysis and other modelling in this paper are mainly determined at low pressures and extrapolated to high pressures outside of the PT range of the experimental database. Although this is commonly safe to do for siderophile element partitioning (e.g., Righter, 2015, 2016), it is best to calibrate the partitioning expression with data that cover the entire PT range relevant to Earth. In the case of sulfide/silicate data, it is currently necessary to utilize the lower pressure datasets of Mungall and Brenan (2014) and Laurenz et al. (2016) for modelling processes that occurred at higher pressures. Therefore, future studies at high PT conditions would be of great value in testing the conclusions of this study.

Finally, aspects of HSE partitioning must be explored in detail. The three post core formation models considered here – addition of a metal-bearing late veneer, segregation of a late sulfide matte, and a combination of late sulfide matte plus a late (metal-free veneer) - all have potential to explain aspects of Earth mantle geochemistry. However, thorough evaluation of all three suffers nonetheless from lack of appropriate data. Much of the quantitative modelling relies on Au, Pd, and Pt, for which we have the most experimental data and the best understanding. But a more complete and thorough understanding will be gained by including all the HSE in quantitative modelling. We know that Re is affected by Fe-Si alloys (Righter et al., 2018), but the extent to which the other HSE – Ru, Rh, Ir, Os – are affected by Fe-Si and Fe-O alloys and their potential for high solubilities in a deep magma ocean setting, needs to be evaluated. Similarly, studies of Re-Pt-Os, which are part of isotopic systems that offer important constraints on hypothesis (e.g., Walker, 2016), should include experiments with all three elements simultaneously to most effectively evaluate the isotopic constraints. Finally, evaluation of multiple mechanisms will be important for gaining the best understanding of the origin of mantle HSE contents - it is possible that multiple mechanisms may be required to explain all the HSE. For example, Righter (2005) proposed that Au, Pd, and Pt might be de-coupled from the other HSE where the former could be established by metal-silicate equilibrium, and the latter by late accretion processes. Although this idea now seems unlikely due to the large effects documented here, the idea that HSE may be de-coupled is a potentially valuable one and shows that one single mechanism may not explain all HSE.

ACKNOWLEDGEMENTS

This work was supported by an RTOP from the NASA Cosmochemistry program to KR. We thank A. Peslier for her assistance with the electron microprobe at JSC. LA-ICP-MS analysis at FSU was supported by NASA grants to MH. Discussions with colleagues at the ELSI Magma Oceanology workshop helped to formulate and sharpen the ideas and issues discussed in this paper.

APPENDIX A. SUPPLEMENTARY MATERIAL

Supplementary data associated with this article can be found, in the online version, at https://doi.org/10.1016/j.gca.2018.04.011.

REFERENCES

Andrault D., Bolfan-Casanova N., Lo Nigro G., Bouhifd M. A., Garbarino G. and Mezouar M. (2011) Solidus and liquidus profiles of chondritic mantle: Implication for melting of the Earth across its history. *Earth Planet. Sci. Lett.* **304**, 251–259.

Badro J., Fiquet G., Guyot F., Gregoryanz E., Occelli F., Antonangeli D. and d'Astuto M. (2007) Effect of light elements on the sound velocities in solid iron: implications for the composition of Earth's core. *Earth Planet. Sci. Lett.* **254**, 233–238.

Ballhaus C., Fonseca R. O., Münker C., Rohrbach A., Nagel T., Speelmanns I. M. and Heuser A. (2017) The great sulfur depletion of Earth's mantle is not a signature of mantle–core equilibration. *Contrib. Miner. Petrol.* **172**, 68–81.

Bennett N. R., Brenan J. M. and Fei Y. (2016) Thermometry of the magma ocean: Controls on the metal–silicate partitioning of gold. *Geochim. Cosmochim. Acta* **184**, 173–192.

Blanchard I., Badro J., Siebert J. and Ryerson F. J. (2015) Composition of the core from gallium metal–silicate partitioning experiments. *Earth Planet. Sci. Lett.* **427**, 191–201.

Boujibar A., Andrault D., Bouhifd M. A., Bolfan-Casanova N., Devidal J. L. and Trcera N. (2014) Metal–silicate partitioning of sulphur, new experimental and thermodynamic constraints on planetary accretion. *Earth Planet. Sci. Lett.* **391**, 42–54.

Brenan J. M. and McDonough W. F. (2009) Core formation and metal–silicate fractionation of osmium and iridium from gold. *Nat. Geosci.* **2**, 798–801.

Burkhardt C., Kleine T., Oberli F., Pack A., Bourdon B. and Wieler R. (2011) Molybdenum isotope anomalies in meteorites: constraints on solar nebula evolution and origin of the Earth. *Earth Planet. Sci. Lett.* **312**, 390–400.

Capobianco C. J., Drake M. J. and de'Aro J. (1999) Siderophile geochemistry of Ga, Ge, and Sn: cationic oxidation states in silicate melts and the effect of composition in iron–nickel alloys. *Geochim. Cosmochim. Acta* **63**, 2667–2677.

Chabot N. L., Campbell A. J., Jones J. H., Humayun M. and Lauer H. V. (2006) The influence of carbon on trace element partitioning behavior. *Geochim. Cosmochim. Acta* **70**, 1322–1335.

Chabot N. L., Safko T. M. and McDonough W. F. (2010) Effect of silicon on trace element partitioning in iron-bearing metallic melts. *Meteorit. Planet. Sci.* **45**, 1243–1257.

Chabot N. L., Wollack E. A., Humayun M. and Shank E. M. (2015) The effect of oxygen as a light element in metallic liquids on partitioning behavior. *Meteorit. Planet. Sci.* **50**, 530–546.

Chi H., Dasgupta R., Duncan M. S. and Shimizu N. (2014) Partitioning of carbon between Fe-rich alloy melt and silicate melt in a magma ocean – Implications for the abundance and origin of volatiles in Earth, Mars, and the Moon. *Geochim. Cosmochim. Acta* **139**, 447–471.

Chou, C. L. (1978) Fractionation of siderophile elements in the Earth's upper mantle. In: Proceedings 9th Lunar and Planetary Science Conference.

Chou C. L., Shaw D. M. and Crocket J. H. (1983) Siderophile trace elements in the Earth's oceanic crust and upper mantle. *J. Geophys. Res. Solid Earth* **88**(S02).

Corgne A., Keshav S., Wood B. J., McDonough W. F. and Fei Y. (2008) Metal–silicate partitioning and constraints on core composition and oxygen fugacity during Earth accretion. *Geochim. Cosmochim. Acta* **72**, 574–589.

Dauphas N., Davis A. M., Marty B. and Reisberg L. (2004) The cosmic molybdenum–ruthenium isotope correlation. *Earth Planet. Sci. Lett.* **226**, 465–475.

Davis F. A., Humayun M., Hirschmann M. M. and Cooper R. S. (2013) Experimentally determined mineral/melt partitioning of first-row transition elements (FRTE) during partial melting of peridotite at 3 GPa. *Geochim. Cosmochim. Acta* **104**, 232–260.

Deguen R., Landeau M. and Olson P. (2014) Turbulent metal–silicate mixing, fragmentation, and equilibration in magma oceans. *Earth Planet. Sci. Lett.* **391**, 274–287.

Ding S., Dasgupta R. and Tsuno K. (2014) Sulfur concentration of martian basalts at sulfide saturation at high pressures and temperatures–implications for deep sulfur cycle on Mars. *Geochim. Cosmochim. Acta* **131**, 227–246.

Ertel W., Walter M. J., Drake M. J. and Sylvester P. J. (2006) Experimental study of platinum solubility in silicate melt to 14 GPa and 2273 K: Implications for accretion and core formation in Earth. *Geochim. Cosmochim. Acta* **70**, 2591–2602.

Fiquet G., Auzende A. L., Siebert J., Corgne A., Bureau H., Ozawa H. and Garbarino G. (2010) Melting of peridotite to 140 gigapascals. *Science* **329**, 1516–1518.

Fischer R. A., Nakajima Y., Campbell A. J., Frost D. J., Harries D., Langenhorst F. and Rubie D. C. (2015) High pressure metal-silicate partitioning of Ni Co, V, Cr, Si, and O. *Geochim. Cosmochim. Acta* **167**, 177–194.

Fischer-Gödde M. and Kleine T. (2017) Ruthenium isotopic evidence for an inner Solar System origin of the late veneer. *Nature* **541**, 525–528.

Gaboardi M. and Humayun M. (2009) Elemental fractionation during LA-ICP-MS analysis of silicate glasses: Implications for matrix-independent standardization. *J. Anal. At. Spectrom.* **24**, 1188–1197.

Georg R. B., Halliday A. N., Schauble E. A. and Reynolds B. C. (2007) Silicon in the Earth's core. *Nature* **447**, 1102–1106.

Hart S. R. and Gaetani G. A. (2016) Experimental determination of Pb partitioning between sulfide melt and basalt melt as a function of P, T and X. *Geochim. Cosmochim. Acta* **185**, 9–20.

Haughton D. R., Roeder P. L. and Skinner B. J. (1974) Solubility of sulfur in mafic magmas. *Econ. Geol.* **69**, 451–467.

Hirose K., Labrosse S. and Hernlund J. (2013) Composition and state of the core. *Annu. Rev. Earth Planet. Sci.* **41**, 657–691.

Holzheid A. and Grove T. L. (2002) Sulfur saturation limits in silicate melts and their implications for core formation scenarios for terrestrial planets. *Am. Mineral.* **87**, 227–237.

Holzheid A. and Palme H. (1996) The influence of FeO on the solubilities of cobalt and nickel in silicate melts. *Geochim. Cosmochim. Acta* **60**, 1181–1193.

Holzheid A., Palme H. and Chakraborty S. (1997) The activities of NiO, CoO and FeO in silicate melts. *Chem. Geol.* **139**, 21–38.

Holzheid A., Sylvester P., O'Neill H. S. C., Rubie D. C. and Palme H. (2000) Evidence for a late chondritic veneer in the Earth's mantle from high-pressure partitioning of palladium and platinum. *Nature* **406**, 396–399.

Humayun M. (2012) Chondrule cooling rates inferred from diffusive profiles in metal lumps from the Acfer 097 CR2 chondrite. *Meteorit. Planet. Sci.* **47**, 1191–1208.

Humayun M., Simon S. B. and Grossman L. (2007) Tungsten and hafnium distribution in calcium–aluminum inclusions (CAIs) from Allende and Efremovka. *Geochim. Cosmochim. Acta* **71**, 4609–4627.

Jochum K. P., Weis U., Stoll B., Kuzmin D., Yang Q., Raczek I., Jacob D. E., Stracke A., Birbaum K., Frick D. A., Günther D. and Enzweiler J. (2011) Determination of reference values for NIST SRM 610–617 glasses following ISO guidelines. *Geostand. Geoanal. Res.* **35**, 397–429.

Kendall J. and Melosh H. J. (2016) Differentiated planetesimal impacts into a terrestrial magma ocean: fate of the iron core. *Earth Planet. Sci. Lett.* **448**, 24–33.

Kimura K. A. N., Lewis R. S. and Anders E. (1974) Distribution of gold and rhenium between nickel-iron and silicate melts: implications for the abundance of siderophile elements on the Earth and Moon. *Geochim. Cosmochim. Acta* **38**, 683–701.

Kiseeva E. S. and Wood B. J. (2013) A simple model for chalcophile element partitioning between sulphide and silicate liquids with geochemical applications. *Earth Planet. Sci. Lett.* **383**, 68–81.

Labidi J., Cartigny P. and Moreira M. (2013) Non-chondritic sulphur isotope composition of the terrestrial mantle. *Nature* **501**, 208–211.

Laurenz V., Rubie D. C., Frost D. J. and Vogel A. K. (2016) The importance of sulfur for the behaviour of highly-siderophile elements during Earth's differentiation. *Geochim. Cosmochim. Acta* **194**, 123–138.

Lewis R. D., Lofgren G. E., Franzen H. F. and Windom K. E. (1993) The effect of Na vapor on the Na content of chondrules. *Meteoritics* **28**, 622–628.

Li J. and Agee C. B. (2001) Element partitioning constraints on the light element composition of the Earth's core. *Geophys. Res. Lett.* **28**, 81–84.

Li Y. and Audétat A. (2015) Effects of temperature, silicate melt composition, and oxygen fugacity on the partitioning of V, Mn Co, Ni, Cu, Zn, As, Mo, Ag, Sn, Sb, W, Au, Pb, and Bi between sulfide phases and silicate melt. *Geochim. Cosmochim. Acta* **162**, 25–45.

Lin J. F., Struzhkin V. V., Sturhahn W., Huang E., Zhao J. Y., Hu M. Y., Alp E. E., Mao H. K., Boctor N. and Hemley R. J. (2003) Sound velocities of iron–nickel and iron–silicon alloys at high pressures. *Geophys. Res. Lett.* **30**(21).

Lupis, C. H. (1983) Chemical thermodynamics of materials. Elsevier Science Publishing Co., Inc., 581 pp.

Ma Z. (2001) Thermodynamic description for concentrated metallic solutions using interaction parameters. *Metall. Mater. Trans. B* **32**, 87–103.

Malavergne V., Charon E., Jones J., Cordier P., Righter K., Deldicque D. and Hennet L. (2016) The formation of nuggets of highly siderophile elements in quenched silicate melts at high temperatures: Before or during the silicate quench? *Earth Planet. Sci. Lett.* **434**, 197–207.

Mao Z., Lin J.-F., Liu J., Alatas A., Gao L., Zhao J. and Mao H.-K. (2012) Sound velocities of Fe and Fe-Si alloy in the Earth's core. *Proc. Natl. Acad. Sci.* **109**, 10239–10244.

Mann U., Frost D. J., Rubie D. C., Becker H. and Audétat A. (2012) Partitioning of Ru, Rh, Pd, Re, Ir and Pt between liquid metal and silicate at high pressures and high temperatures-Implications for the origin of highly siderophile element concentrations in the Earth's mantle. *Geochim. Cosmochim. Acta* **84**, 593–613.

Marchi S., Canup R. M. and Walker R. J. (2018) Heterogeneous delivery of silicate and metal to the Earth by large planetesimals. *Nat. Geosci.* **11**, 77–82.

Medard E., Schmidt M. W., Wälle M., Keller N. S. and Günther D. (2015) Platinum partitioning between metal and silicate melts: Core formation, late veneer and the nanonuggets issue. *Geochim. Cosmochim. Acta* **162**, 183–201.

Medard, E., Martin, A. M., Righter, K., Lanziroti, A., and Newville, M. (2016) Platinum partitioning at low oxygen fugacity: implications for core formation processes. In 47th Lunar and Planetary Science Conference, abstract # 2801.

Michely L. T., Leitzke F. P., Speelmanns I. M. and Fonseca R. O. C. (2017) Competing effects of crystal chemistry and silicate melt composition on trace element behavior in magmatic systems: insights from crystal/silicate melt partitioning of the REE, HFSE, Sn, In, Ga, Ba, Pt and Rh. *Contrib. Miner. Petrol.* **172**, 39–61.

Morgan J. W. (1986) Ultramafic xenoliths: clues to Earth's late accretionary history. *J. Geophys. Res. Solid Earth* **91**(B12), 12375–12387.

Mungall J. E. and Brenan J. M. (2014) Partitioning of platinum-group elements and Au between sulfide liquid and basalt and the origins of mantle-crust fractionation of the chalcophile elements. *Geochim. Cosmochim. Acta* **125**, 265–289.

Newsom H. E. and Drake M. J. (1983) Experimental investigation of the partitioning of phosphorus between metal and silicate phases: Implications for the Earth, Moon and eucrite parent body. *Geochim. Cosmochim. Acta* **47**, 93–100.

O'Neill H. S. C. (1991) The origin of the Moon and the early history of the Earth—A chemical model. Part 2: The Earth. *Geochim. Cosmochim. Acta* **55**, 1159–1172.

Olesinski R. W. and Abbaschian G. J. (1985) The Si-Zn (Silicon-Zinc) system. *Bull. Alloy Phase Diagrams* **6**, 545–548.

Palme, H. and O'Neill, H.S.C. (2014) Cosmochemical estimates of mantle composition. Treatise on Geochemistry, 2 (second ed.), pp. 1–39.

Ricolleau A., Fei Y., Corgne A., Siebert J. and Badro J. (2011) Oxygen and silicon contents of Earth's core from high pressure metal–silicate partitioning experiments. *Earth Planet. Sci. Lett.* **310**, 409–421.

Righter K. (2005) Highly siderophile elements: constraints on Earth accretion and early differentiation. *Earth's Deep Mantle: Struct., Compos. Evol.*, 201–218.

Righter K. (2011) Prediction of metal–silicate partition coefficients for siderophile elements: an update and assessment of PT conditions for metal–silicate equilibrium during accretion of the Earth. *Earth Planet. Sci. Lett.* **304**, 158–167.

Righter K. (2015) Modeling siderophile elements during core formation and accretion, and the role of the deep mantle and volatiles. *Am. Mineral.* **100**, 1098–1109.

Righter K. (2016) Metal-silicate partitioning of siderophile elements and core-mantle segregation, deep earth: physics and chemistry of the lower mantle and core. *Geophysical Monograph* **217**, 161–174.

Righter K. and Drake M. J. (2000) Metal-silicate equilibrium in the early Earth: new constraints from volatile moderately siderophile elements Ga, Sn, Cu and P. *Geochim. Cosmochim. Acta* **64**, 3581–3597.

Righter K. and Ghiorso M. S. (2012a) Redox systematics of a magma ocean with variable pressure-temperature gradients and composition. *Proc. Nat. Acad. Sci.* **109**, 11955–11960.

Righter K. and Ghiorso M. S. (2012b) Correction for Righter and Ghiorso, Redox systematics of a magma ocean with variable pressure-temperature gradients and composition. *Proc. Nat. Acad. Sci.* **109**, 16749–16750.

Righter K., Drake M. J. and Yaxley G. (1997) Prediction of siderophile element metal-silicate partition coefficients to 20 GPa and 2800 C: the effects of pressure, temperature, oxygen fugacity, and silicate and metallic melt compositions. *Phys. Earth Planet. Inter.* **100**, 115–134.

Righter K., Humayun M. and Danielson L. R. (2008) High pressure and temperature partitioning of palladium during core formation. *Nat. Geosci.* **1**, 321–323.

Righter K., Pando K. and Danielson L. R. (2009) Experimental evidence for sulfur-rich martian magmas: Implications for volcanism and surficial sulfur sources. *Earth Planet. Sci. Lett.* **288**, 235–243.

Righter K., Pando K., Danielson L. R. and Lee C.-T. (2010) Partitioning of Mo, P and other siderophile elements (Cu, Ga, Sn, Ni Co, Cr, Mn, V, W) between metal and silicate melt as a function of temperature and melt composition. *Earth Planet. Sci. Lett.* **291**, 1–9.

Righter K., Danielson L. R., Pando K., Williams J., Humayun M., Hervig R. L. and Sharp T. G. (2015) Mantle HSE abundances in Mars due to core formation at high pressure and temperature. *Met Planet. Sci.* **50**, 604–631.

Righter K., Danielson L. R., Pando K. M., Shofner G. A., Sutton S. R., Newville M. and Lee C. T. (2016) Valence and metal/silicate partitioning of Mo: Implications for conditions of Earth accretion and core formation. *Earth Planet. Sci. Lett.* **437**, 89–100.

Righter, K., Pando, K., Danielson, L. R., Humayun, M., Righter, M., Lapen, T., & Boujibar, A. (2016). Effect of Silicon on Activity Coefficients of Siderophile Elements (P, Au, Pd, As, Ge, Sb, and In) in Liquid Fe, with Application to Core Formation. In 47th Lunar and Planetary Science Conference, abstract #2116.

Righter K., Nickodem K., Pando K., Danielson L., Boujibar A., Righter M. and Lapen T. J. (2017) Distribution of Sb, As, Ge, and In between metal and silicate during accretion and core formation in the Earth. *Geochim. Cosmochim. Acta* **198**, 1–16.

Righter, K., Pando, K., Yang, S., Humayun, M. (2018) Effect of silicon on the activity coefficient of Rhenium in Fe-Si liquids: implications for HSE and Os isotopes in planetary mantles. In 49th Lunar Planetary Science Conference, abstract # 2484.

Rubie D. C., Frost D. J., Mann U., Asahara Y., Nimmo N., Tsuno K., Kegler P., Holzheid A. and Palme H. (2011) Heterogeneous accretion, composition and core–mantle differentiation of the Earth. *Earth Planet. Sci. Lett.* **301**, 31–42.

Rubie D. C., Laurenz V., Jacobson S. A., Morbidelli A., Palme H., Vogel A. K. and Frost D. J. (2016) Highly siderophile elements were stripped from Earth's mantle by iron sulfide segregation. *Science* **353**, 1141–1144.

Sanloup C., Fiquet G., Gregoryanz E., Morard G. and Mezouar M. (2004) Effect of Si on liquid Fe compressibility: Implications for sound velocity in core materials. *Geophys. Res. Lett.* **31**(7).

Schönbächler M., Carlson R. W., Horan M. F., Mock T. D. and Hauri E. H. (2010) Heterogeneous accretion and the moderately volatile element budget of Earth. *Science* **328**, 884–887.

Sharp M., Righter K. and Walker R. J. (2015) Estimation of trace element concentrations in the lunar magma ocean using mineral-and metal-silicate melt partition coefficients. *Meteorit. Planet. Sci.* **50**, 733–758.

Siebert J., Badro J., Antonangeli D. and Ryerson F. J. (2013) Terrestrial accretion under oxidizing conditions. *Science* **339**, 1194–1197.

Siebert J., Corgne A. and Ryerson F. J. (2011) Systematics of metal–silicate partitioning for many siderophile elements applied to Earth's core formation. *Geochim. Cosmochim. Acta* **75**, 1451–1489.

Solomatov V. S. (2007) Magma oceans and primordial mantle differentiation. *Treatise Geophys.* **9**, 91–120.

Steelmaking J. (1988) *Steelmaking Data Sourcebook*. Gordon and Breach Science Publishers, Montreux.

Steenstra, E.S., Putter, R., Seegers, A.X., Lin, Y.H., & van Westrenen, W. (2017) Significant non-linear pressure effects on interaction coefficients of siderophile elements in FeSi alloys: implications for geochemical models of core formation in the earth. In Lunar and Planetary Science Conference (vol. 48, LPSC).

Suer T. A., Siebert J., Remusat L., Menguy N. and Fiquet G. (2017) A sulfur-poor terrestrial core inferred from metal–silicate partitioning experiments. *Earth Planet. Sci. Lett.* **469**, 84–97.

Tuff J., Wood B. J. and Wade J. (2011) The effect of Si on metal-silicate partitioning of siderophile elements and implications for the conditions of core formation. *Geochim. Cosmochim. Acta* **75**, 673–690.

Wade J. and Wood B. J. (2005) Core formation and the oxidation state of the Earth. *Earth Planet. Sci. Lett.* **236**, 78–95.

Wade J., Wood B. J. and Tuff J. (2012) Metal–silicate partitioning of Mo and W at high pressures and temperatures: evidence for late accretion of sulphur to the Earth. *Geochim. Cosmochim. Acta* **85**, 58–74.

Walker R. J. (2016) Siderophile elements in tracing planetary formation and evolution. *Geochem. Perspect.* **5**, 36–66.

Walker R. J., McDonough W. F., Honesto J., Chabot N. L., McCoy T. J., Ash R. D. and Bellucci J. J. (2008) Modeling fractional crystallization of group IVB iron meteorites. *Geochim. Cosmochim. Acta* **72**, 2198–2216.

Wang Z. and Becker H. (2013) Ratios of S, Se and Te in the silicate Earth require a volatile-rich late veneer. *Nature* **499**, 328–331.

Wasson J. T., Ouyang X., Wang J. and Eric J. (1989) Chemical classification of iron meteorites: XI. Multi-element studies of 38 new irons and the high abundance of ungrouped irons from Antarctica. *Geochim. Cosmochim. Acta* **53**, 735–744.

Wheeler K. T., Walker D. and McDonough W. F. (2011) Pd and Ag metal-silicate partitioning applied to Earth differentiation and core-mantle exchange. *Meteorit. Planet. Sci.* **46**, 199–217.

Wood B. J. (2008) Accretion and core formation: constraints from metal–silicate partitioning. *Philos. Trans. R. Soc. London A: Math., Phys. Eng. Sci.* **366**, 4339–4355.

Wood B. J., Walter M. J. and Wade J. (2006) Accretion of the Earth and segregation of its core. *Nature* **441**, 825–833.

Wood B. J., Kiseeva E. S. and Mirolo F. J. (2014) Accretion and core formation: The effects of sulfur on metal–silicate partition coefficients. *Geochim. Cosmochim. Acta* **145**, 248–267.

Yang S., Humayun M., Righter K., Jefferson G., Fields D. and Irving A. J. (2015) Siderophile and chalcophile element abundances in shergottites: Implications for Martian core formation. *Meteorit. Planet. Sci.* **50**, 691–714.

Ziegler K., Young E. D., Schauble E. A. and Wasson J. T. (2010) Metal–silicate silicon isotope fractionation in enstatite meteorites and constraints on Earth's core formation. *Earth Planet. Sci. Lett.* **295**, 487–496.

Associate editor: Richard J. Walker